Master's Thesis

THz Modulators Based on AlGaN/GaN High Electron Mobility Transistors

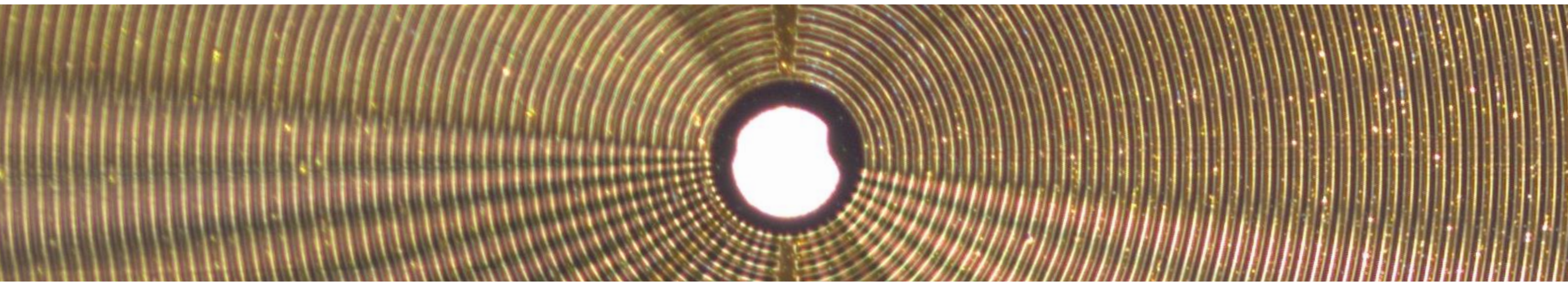

29^{th} of May 2019

Anne Landgrebe-Christiansen
Jacob Nørkjær Schunck

AALBORG UNIVERSITY
STUDENT REPORT

Department of
Materials and Production
Skjernvej 4A
9220 Aalborg East
http://www.mp.aau.dk

Title:
THz Modulators Based on AlGaN/GaN High Electron Mobility Transistors

Project:
Master's Thesis

Project Period:
February 2019 - May 2019

Authors:
Anne Landgrebe-Christiansen
Jacob Nørkjær Schunck

Supervisor:
Vladimir Popok

Number of Pages: 69
Finished: 29-05-2019

Abstract:

The objective of this project is to design and fabricate THz modulators based on the AlGaN/GaN HEMT technology. Therefore, the fundamentals of FETs are described with a focus on AlGaN/GaN-based HEMTs. In this regard, the formation of a two-dimensional electron gas (2DEG) conducting channel and fabrication of proper electrical contacts are discussed. The dispersion relations of plasma waves in the 2DEG conduction channel of a FET are described in order to explain the coupling between them and THz radiation. Different types of AlGaN/GaN-based THz modulators presented in the literature are analysed, in order to determine which design is preferable in regards to available equipment and relevant time frame of the project. Based on this survey, circular grating-gate structures are chosen, designed, and fabricated in collaboration with Twente University in the Netherlands. Comprehensive electrical characterisation of these devices reveals appropriate transistor-like behaviour making it very promising to obtain THz modulation properties. Unfortunately, we did not succeed to examine THz modulation due to difficulties with wire bonding of individual devices into arrays and connection to the external electrical circuit. Consequently, THz spectroscopy measurements could not be performed.

Preface

This Master's thesis is produced by two physics students at Aalborg University. The main goal is to design and fabricate THz modulators for electrical characterisation and THz spectroscopy in order to determine the resonant frequency and modulation depth of these devices. The requisites for reading this thesis is a fundamental knowledge of surface science and semiconductor physics.

We would like to thank our supervisor Vladimir Popok for his guidance and advice. Furthermore, we would like to thank Lis Karen Nanver and Shivakumar Thammaiah from Twente University for their assistance in design and fabrication of the THz devices.

Reading Guide

Throughout this thesis, there will appear source references which are collected in the bibliography at the end of the report. When a reference to a source with [Source Number] is made, the reference will guide the reader to the bibliography where books are listed with authors, title, edition, year, and publisher, while articles are listed with authors, title, journal, volume, and year. Sources are listed in the same order as they appear in the report. Figures, tables, and equations are numbered with relation to the chapters they appear in, e.g. the first figure in chapter 3 is numbered 3.1, the second 3.2 etc. Explanatory text to each figure is found right below, whereas for tables it is found right above.

Anne Landgrebe-Christiansen   Jacob Nørkjær Schunck

Table of Contents

Chapter 1

Introduction

In resent years, electromagnetic radiation of terahertz (THz) frequencies has gained a lot of scientific attention for its possible implementation in industrial purposes such as astronomical and medical research, material characterisation, security screening, military technology, and much more [1–4]. Even though the potential of applications is immense, devices operating within the THz band are, unlike devices for other frequency realms such as visible light, inferred light, microwaves, radio waves, gamma rays etc., not very extensively explored and developed. The technological advancement relies heavily on the development of efficient and compact THz detectors, emitters, and modulators operating at room-temperature. Unfortunately, the well-optimised technologies operating within the surrounding infrared and millimetre wave frequencies are not directly applicable in the THz band. Therefore, the challenging development of THz technologies requires innovative use of new materials, complex physical theory, and intelligent integration techniques. Nowadays, most of the upcoming THz technologies are on the experimental or even idea stage, however, a few technologies are maturing and playing an increasingly important role in the scientific world [1].

The advantages of using THz radiation are plenty. Firstly, it can penetrate a wide variety of materials such as wood, masonry, paper, plastic, tissue, ceramics, and clothing but has a high absorption in water and metals, making it ideal for e.g. screening of concealed weapons and explosive substances [2]. Besides this, the THz photon energy is around 4.1 meV making it non-ionising, meaning that it is insufficient to break strong covalent bonds and can thus penetrate organic tissue without causing substantial damage [1]. This means that THz radiation is favourable compared to X-rays which are conventionally used for medical or security examinations. Secondly, in spectroscopy, THz radiation can be used to obtain images with a high spatial and temporal resolution compared to micro- and millimetre waves. The smaller wavelength makes for a higher spatial resolution, whereas the short oscillation period allows for a precise image timing, resulting in a high temporal resolution. This is important when the dynamics of molecules and solids are of interest. Besides this, molecular vibration and rotation modes can be investigated using THz radiation since collective excitations, such as plasmons and phonons, have very specific fingerprints in the THz band [1]. Lastly, THz radiation can be utilised for short-ranged wireless communication of high speed and bandwidth. This is due to the merging of electronics and optoelectronics in the THz band [5, 6].

It is inherently not difficult to imagine the potential of THz technology. It is, however, a challenging task to design and fabricate devices which can realise this potential to its fullest. Today, a handful of promising technologies exist, deviating in their applicability, efficiency, and reliability. One of these will be the main focus of this project, namely the one based on the coupling between THz radiation and plasma waves in high electron mobility transistors (HEMTs), which is currently in its initial stage of development. In the year of 1993, M. I. Dyakonov and M. S. Shur theoretically predicted THz emission in gated two-dimensional electron gas (2DEG) devices, such as HEMTs, due to resonant plasma excitations [7]. Only three years later they suggested that the same principles could be utilised to fabricate THz detectors [8]. As the development of the technology has progressed, not only the idea of functioning THz HEMT emitters and detectors has been realised, but also modulators of incoming THz radiation. Such modulators, specifically those consisting of an AlGaN/GaN heterostructure, will be studied theoretically and experimentally throughout this project.

The objective of this project is to understand the physical principles involved in the workings of THz modulators based on AlGaN/GaN HEMTs, and use this knowledge to design functional devices for THz technology. The theoretical foundation will be achieved through obtaining fundamental understanding of how, and under what conditions, the AlGaN/GaN heterostructure results in the formation of a 2DEG, and how this 2DEG can be utilised as a conducting channel in a HEMT. Furthermore, the coupling between THz radiation and plasma waves in the 2DEG will be described, in order to explain how a HEMT can function as a THz modulator. Different design geometries of such described in the literature, will be studied in order to design original devices. The most promising devices will be fabricated for electrical characterisation and THz spectroscopy measurements in order to determine the quality of the devices as well as the resonant frequency and modulation depth, and these results will be compared to the literature.

Chapter 2

Introduction to Field Effect and High Electron Mobility Transistors

One of the biggest breakthroughs in the history of semiconductor technology, and electronics in general, is the invention of the transistor. In December 1947 the first ever transistor was fabricated by William Shockley, John Bardeen, and Walter Brattain at Bell Telephone Laboratories [9]. A transistor is a semiconductor-based electrical component which main purpose is to regulate an electrical signal using a many times smaller signal. For the purpose of this project, the focus of the present chapter will be a specific kind of transistor, namely the Field Effect Transistor (FET). The workings of a FET was first conceptualised by Julius Edgar Lilienfeld in 1930 [10], which later would be realised by the invention and optimisation of the transistor. A FET, which is illustrated in Fig. 2.1, functions as a capacitor where one of the plates, namely the semiconductor, serves as a conducting channel between a source and drain. The other plate, called the gate, controls the amount of charges induced in the channel. By applying a sufficient bias to the gate, charge carriers will be accumulated in the semiconductor at the insulator-semiconductor junction and a current is thus able to flow between the source and drain [10, 11].

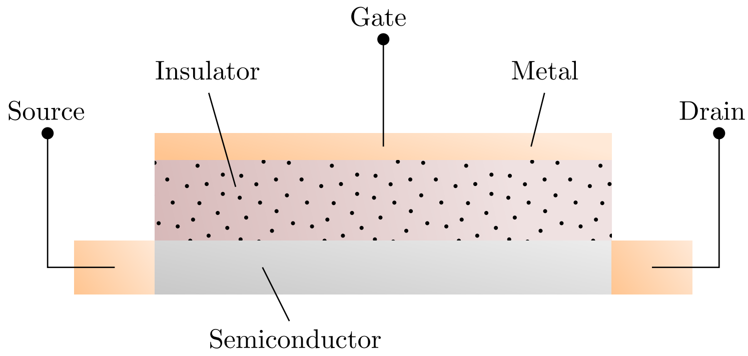

Figure 2.1. Illustration of a typical FET.

This simple principle is utilised in a handful of devices such as the Metal Oxide Semiconductor Field Effect Transistor (MOSFET), the Metal Insulator Semiconductor Field Effect Transistor (MISFET), the Junction Field Effect Transistor (JFET), and finally the extraordinary High Electron Mobility Transistor (HEMT), which will be the focus of the rest of this chapter. Here, the functionality, physical principles, advantages, and limitations of said transistor type will be presented and discussed. The main focus will be AlGaN/GaN-based HEMTs as these are the ones utilised in the experiments of this project.

Generally, it applies for all types of transistors that to function properly it is critical that the channel is connected to the source and drain by ohmic contacts [10], which are not always easy to fabricate for certain semiconductor materials, such as GaN [12, 13]. Therefore, the definition and production of ohmic contacts will be of interest and thus also discussed in this chapter.

2.1 Formation of Two-Dimensional Electron Gas in Heterostructures

This section seeks to explain the physical principles which are necessary for understanding the workings of a HEMT. A HEMT is a heterostructure-based transistor which, as the name suggests, consists of two different semiconductors. For certain combinations of materials, this can result in special electrical effects at their junction. One of these effects is the formation of a two-dimensional electron gas (2DEG), which can be utilised in transistors as a tunable channel with high electron density and fast electrical response. For the purpose of this project, the formation of a 2DEG in an AlGaN/GaN heterostructure will be of main interest throughout this section.

Consider a heterojunction of a wide and a narrower band gap semiconductor such as AlGaN and GaN, respectively. The characteristics of such a junction is highly dependent on the mutual alignment of the band gaps. The different possibilities of alignment and the corresponding names are illustrated in Fig. 2.2. The case of straddling is the most common among heterojunctions [9] and is also the case of AlGaN/GaN, hence only this situation will be further discussed.

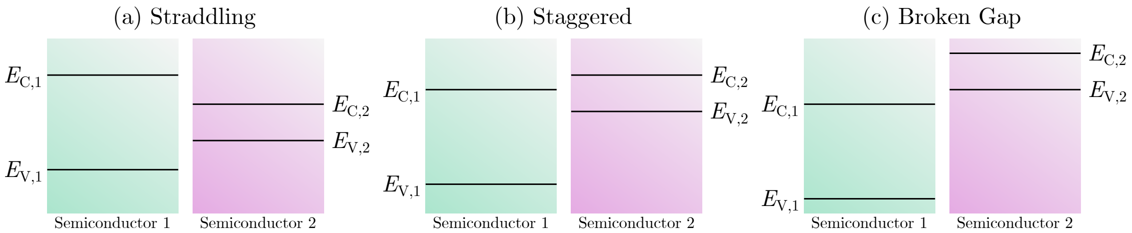

Figure 2.2. Possible band gap alignments for a heterojunction consisting of a wide and a narrower band gap semiconductor. Here, E_{C} is the minimum of the conduction band and E_{V} is the maximum of the valence band.

The formation of a 2DEG is caused by band bending of the energy bands near the interface of the two semiconductors and occurs when the conduction band of one of the semiconductors drops below the Fermi level, E_{F}, for a confined region in space. This acts as a quantum potential well which results in accumulation of electrons in this confined region. For the most cases it is necessary to introduce doping into at least one of the two semiconductors of the heterostructure to facilitate the formation of a 2DEG. However, for AlGaN/GaN heterostructures no intentional doping is required due to the strong spontaneous and piezoelectric polarisation effects at the AlGaN/GaN interface and, therefore, it is possible to form a 2DEG using only intrinsic components [1]. The energy band relations for AlGaN and GaN, before and after electrical contact, are shown in Fig. 2.3. This figure illustrates that discontinuities of the energy bands at the interface lead to a strong electric field, band bending, and the formation of an approximately triangular quantum well, upon electrical contact. Electrons are accumulated in the quantum well and when the few lowest quantum states have been occupied, a quasi 2DEG is formed at the GaN side of the interface [1]. The electrons only have quantised energy along the spatial direction, z, perpendicular to the interface, but are free to move in the other two spatial directions, hence the name *two-dimensional electron gas* [9].

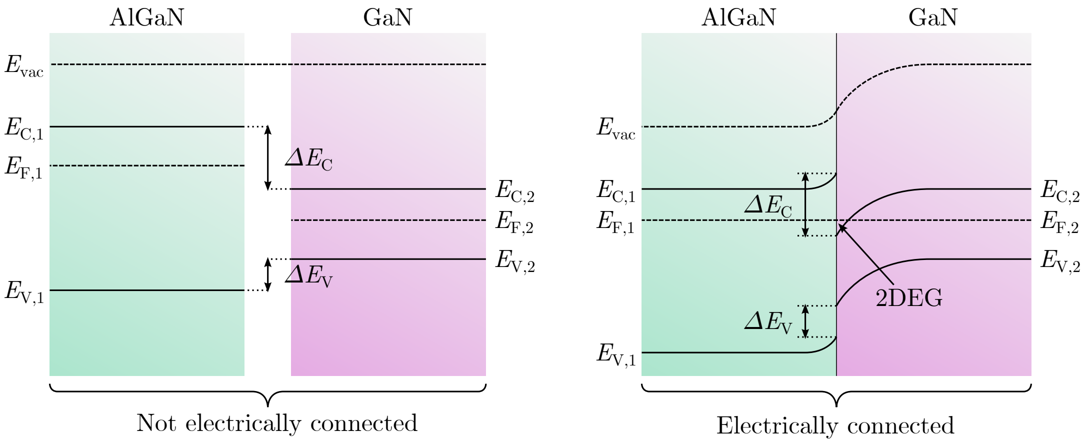

Figure 2.3. Illustration of the energy relations of AlGaN and GaN before and after electrical contact.

Since the relations between the energy bands of AlGaN and GaN determine the properties of the 2DEG, it is obvious that one of the parameters that characterises the 2DEG is the band gap of AlGaN, which is dependent on the content of Al. This dependency can be described as

$$E_{\mathrm{g}}^{\mathrm{AlGaN}}(x) = xE_{\mathrm{g}}^{\mathrm{AlN}} + (1-x)E_{\mathrm{g}}^{\mathrm{GaN}} - x(1-x)1.0\ \mathrm{eV}, \tag{2.1}$$

where x is the content of Al and $E_{\mathrm{g}}^{\mathrm{AlGaN}}(x)$, $E_{\mathrm{g}}^{\mathrm{AlN}} = 6.13$ eV, and $E_{\mathrm{g}}^{\mathrm{GaN}} = 3.42$ eV are the band gaps for AlGaN, AlN, and GaN, respectively [14, 15]. The difference in conduction band minimum between AlGaN and GaN can be written as

$$\Delta E_{\mathrm{C}} = 0.7\left(E_{\mathrm{g}}^{\mathrm{AlGaN}}(x) - E_{\mathrm{g}}^{\mathrm{AlGaN}}(0)\right). \tag{2.2}$$

For AlGaN with a content of 27 % Al, written $Al_{0.27}Ga_{0.73}N$, the difference in conduction band minimum would be $\Delta E_{\mathrm{C}} = 0.53$ eV, which contributes to the formation of a deep quantum well.

2.2 High Electron Mobility Transistors

A HEMT, also known as Heterostructure Field Effect Transistor (HFET) or Two-dimensional Electron Gas Field Effect Transistor (TEGFET), is a transistor utilising the 2DEG of a heterostructure as a conducting channel. A schematic of an AlGaN/GaN-based

HEMT is shown in Fig. 2.4. Here the source and drain are connected through the electron gas, whereas the gate forms a Schottky barrier with the AlGaN layer [1].

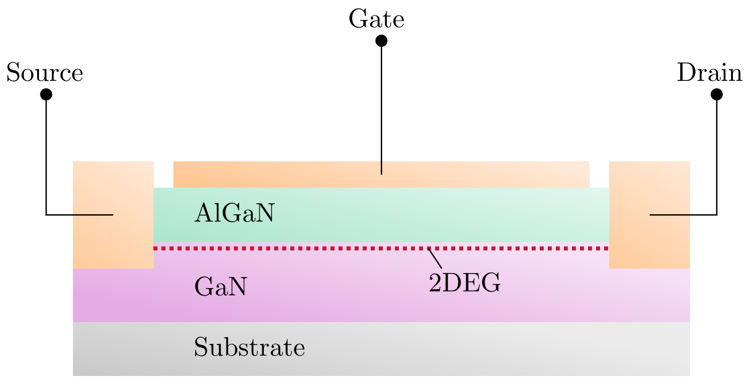

Figure 2.4. Illustration of an AlGaN/GaN-based HEMT.

If no voltage is applied to the gate, a current is able to flow between the source and drain using the 2DEG channel. By adjusting the gate bias the quantum well is either raised or lowered in energy which regulates the amount of accumulated electrons. This changes the carrier density of the 2DEG and effectively the resistance in the channel. Hence, a HEMT can be approximated as a variable resistor which is modulated by the gate bias. By applying a sufficient gate voltage, the quantum well is completely emptied which makes the concentration of electrons in the 2DEG negligible and the channel is pinched off [1, 9, 10]. The corresponding gate voltage is called the threshold voltage and is denoted V_{th}.

From the gradual channel approximation, which assumes that the voltage varies gradually from the source to the drain, the source-to-drain current of a HEMT, and a FET in general, can be expressed as

$$I_{\mathrm{sd}} = -en_{\mathrm{s}}vW, \tag{2.3}$$

where e is the elementary charge, n_{s} is the charge density, v is the drift velocity of free electrons in the gated channel, and W is the gate width [1, 10]. The negative sign is due to the negative charge of electrons. The dependency between the charge density in the channel and the tunable gate bias can be described by

$$n_{\mathrm{s}} = \frac{C_{\mathrm{g}}\left(V_{\mathrm{g}} - V_{\mathrm{th}}\right)}{e}, \tag{2.4}$$

where C_{g} is the effective gate-to-channel capacitance per unit area [1]. Let x denote a position in the spatial direction directly between the source and drain. By applying a source-drain voltage, V_{sd}, the charge density at position x can be described by

$$n_{\mathrm{s}}(x) = \frac{C_{\mathrm{g}}\left(V_{\mathrm{g}} - V_x - V_{\mathrm{th}}\right)}{e}. \tag{2.5}$$

Here V_x describes the channel potential which varies from 0 to V_{sd} between $x = 0$ and $x = L$, where L is the gate length. By substituting this equation into Eq. (2.3) the following expression is obtained,

$$I_{\mathrm{sd}} = -WC_{\mathrm{g}}\left(V_{\mathrm{g}} - V_x - V_{\mathrm{th}}\right)v. \tag{2.6}$$

From this equation it seems that the source-drain current varies through the channel as V_x changes, however, this is not the case since the current is constant in a series circuit. This equation merely describes the source-drain current for a specific V_x. To obtain an equation that describes the source-drain current when the charge density varies through the channel due to an applied source-drain bias, this equation has to be integrated over every value of V_x. But first, some small details have to be taken into account. The electron drift velocity is given by $v = \mu E(x)$, where μ is the electron mobility and $E(x) = -\frac{\mathrm{d}V_x}{\mathrm{d}x}$ is the electric field in the x-direction. This can be substituted into Eq. (2.6) to yield

$$I_{\mathrm{sd}} = \mu W C_{\mathrm{g}} \left(V_{\mathrm{g}} - V_x - V_{\mathrm{th}}\right) \frac{\mathrm{d}V_x}{\mathrm{d}x}. \tag{2.7}$$

By dividing by L on both sides and using the earlier mentioned boundaries at the source and drain, $V_x(0) = 0$ and $V_x(L) = V_{\mathrm{sd}}$, the equation can be integrated in the following manner,

$$\frac{1}{L} \int_{x=0}^{L} I_{\mathrm{sd}} \,\mathrm{d}x = \frac{\mu W C_{\mathrm{g}}}{L} \int_{V_x=0}^{V_{\mathrm{sd}}} \left(V_{\mathrm{g}} - V_x - V_{\mathrm{th}}\right) \mathrm{d}V_x, \tag{2.8}$$

which yields that

$$I_{\mathrm{sd}} = \frac{\mu W C_{\mathrm{g}}}{L} \left(\left(V_{\mathrm{g}} - V_{\mathrm{th}}\right) V_{\mathrm{sd}} - \frac{1}{2} V_{\mathrm{sd}}^2 \right). \tag{2.9}$$

From this derived equation it is seen that the source-drain current is not only dependant on the gate voltage but also the source-drain voltage. The source-drain current as a function of the source-drain voltage for a constant gate voltage is called the output characteristic curve, whereas the source-drain current as a function of the gate voltage for a constant source-drain voltage is called the transfer characteristic curve. In [1] both have been measured for an AlGaN/GaN-based HEMT with $L = 2$ µm and $W = 4$ µm, which is shown in Fig. 2.5.

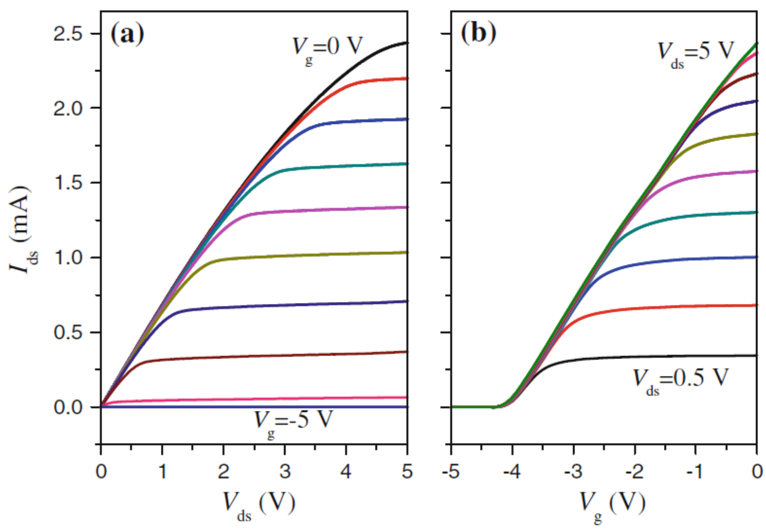

Figure 2.5. The (a) output and (b) transfer characteristic curve for a AlGaN/GaN-based HEMT with $L = 2$ µm and $W = 4$ µm. Adopted from [1].

From Fig. 2.5(a) it is seen that the source-drain current becomes saturated for a given source-drain voltage, named the saturation voltage, V_{sat}. This saturation voltage is increasing for higher gate voltages. From Fig. 2.5(b) it is seen that the threshold voltage for this HEMT is approximately $V_{\mathrm{th}} = -4.1$ V, obviously independent of the source-drain voltage.

2.2.1 Critical Thickness of AlGaN

An important parameter to consider regarding AlGaN/GaN-based HEMTs is the thickness of the AlGaN barrier layer. For an intrinsic AlGaN/GaN sample, the strong piezoelectric and spontaneous polarisation effects play an important role in the formation of a 2DEG and characterises the dependency between thickness of the AlGaN layer and electron density in the 2DEG. In this section, a theoretical explanation of this phenomenon will be presented along with experimental evidence.

In [16], a theoretical explanation based on simple electrostatics is given. Here, Ibbetson et al. suggest that the charge balance between the surface, AlGaN barrier layer, and 2DEG can be described by

$$\sigma_{\mathrm{surface}} + \sigma_{\mathrm{AlGaN}} - en_{\mathrm{s}} = 0. \tag{2.10}$$

Here, $\sigma_{\mathrm{surface}}$ is the charge due to ionised surface states and σ_{AlGaN} is the charge due to ionised donors in the AlGaN barrier caused by doping. Hence, for an undoped AlGaN barrier it applies that $\sigma_{\mathrm{AlGaN}} = 0$. It is implied that the 2DEG is not caused by electrons thermally generated in the GaN buffer layer, which would result in a positive space charge in this layer [16], and hence no σ_{GaN} is present in Eq. (2.10). Consider a donor-like surface state, where donor-like should be understood in the sense that it is neutral when occupied and positive when emptied. When the energy of the state is below the Fermi level, it does not contribute to the 2DEG since $\sigma_{\mathrm{surface}} = en_{\mathrm{s}} = 0$. By increasing the thickness of the barrier layer, the energy of this surface state rises. When its energy reaches the Fermi level, electrons are then able to transfer from the surface state into the unoccupied states in the quantum well, leaving behind a positive surface charge [16–18]. The thickness of the barrier for which the surface states reach the Fermi level is called the critical thickness, t_{CR}, which marks the point from which the 2DEG starts to form. It was found that the 2DEG density as a function of barrier thickness could be described by

$$qn_{\mathrm{s}} = \sigma_{\mathrm{P}} \left(1 - \frac{t_{\mathrm{CR}}}{t}\right), \tag{2.11}$$

where t is the thickness of the AlGaN barrier layer, q is the charge, and σ_{P} is the polarisation-induced charge [16]. Hall measurements of electron density in a 2DEG as a function of barrier thickness was performed by Ibbetson et al. and is shown in Fig. 2.6.

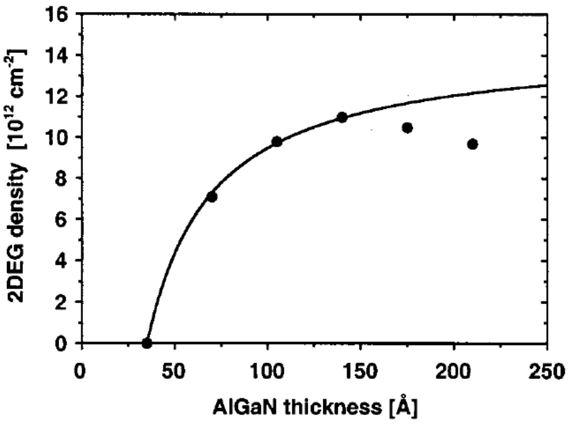

Figure 2.6. Measurements of electron concentration in 2DEG as a function of $Al_{0.34}Ga_{0.64}N$ layer thickness, for a AlGaN/GaN sample at room temperature. The regression is made using Eq. (2.11) for points with t < 150 Å. Adopted from [16].

Here, the regression is made using least squares fit of Eq. (2.11) for measurements where t < 150 Å. From this figure it is seen that the 2DEG density increases drastically once the critical thickness of around 35 Å has been reached, but becomes saturated, or even decreases, for thicknesses of 130 to 140 Å or higher. When considering these results it is important to note that the 2DEG density is not only dependent on the AlGaN barrier thickness, but also the content of Al.

In [19], a normally-off AlGaN/GaN device with an AlGaN barrier thickness of ~ 3 nm and Al-content of ~ 25 % has been studied. For this device it was found that no 2DEG channel had been formed due to the low thickness of AlGaN, hence it was necessary to apply a high enough gate voltage in order to fill the quantum well with charge carriers. Therefore, this device functions as a normally-off HEMT. In this work it is stated that the critical thickness of a 25 % Al-content AlGaN barrier is around 6 nm.

The formation of a 2DEG in AlGaN/GaN samples were also studied in a previous semester project [20] using Kelvin Probe Force Microscopy (KPFM). The surface potential of samples with different AlGaN barrier thickness were measured in order to map the formation of a 2DEG. The Al-content of all the samples used were ~ 28 %. Some of the results are shown in Fig. 2.7.

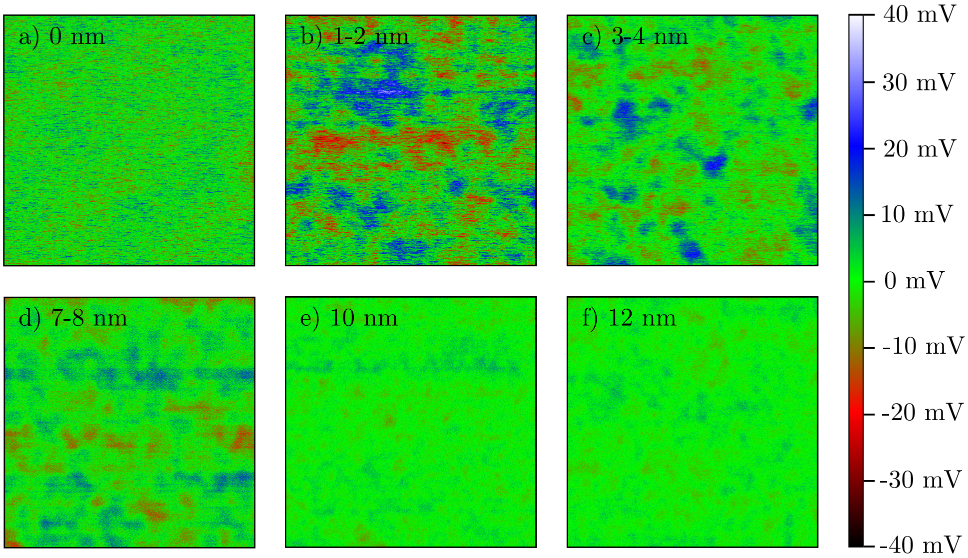

Figure 2.7. Measurements of deviation from the mean surface potential of AlGaN/GaN samples, taken from a previous semester project [20]. The size of all images is 10 μm × 10 μm. The thickness of the AlGaN barrier is given in the top left corner of each image. The mean surface potential of the image regions are given by (a) 0.69 V, (b) 1.04 V, (c) 1.20 V, (d) 1.15 V, (e) 1.25 V, and (f) 1.21 V.

Here, Fig. 2.7(a) shows the homogeneous surface potential of a pure GaN sample. In Fig. 2.7(b) a thin layer of AlGaN has been deposited, resulting in an island-like distribution pattern of the surface potential. This low thickness is not enough to form stoichiometric AlGaN, thus explaining the high deviation in surface potential. From Fig. 2.7(c) and 2.7(d) it is seen how a further increment of AlGaN thickness results in higher mean surface potential and a more mosaic-like distribution pattern with a lower deviation from the mean. This indicates that the critical thickness has been reached and thus the formation of a 2DEG has occurred in local regions of the samples. In Fig. 2.7(e) and 2.7(f) the homogeneous surface potential indicates that a continuous 2DEG with a high electron density has been formed which, therefore, suggests that the 2DEG is fully formed at an AlGaN thickness of around 10 nm. The mean surface potential for these images also indicates that the electron density in the 2DEG has been saturated at this thickness. These results are in great agreement with the ones presented in [16].

2.2.2 Causes and Consequences of Defects

Another important parameter to consider in order to ensure the high mobility of the 2DEG in a HEMT is the formation of defects caused from lattice mismatch and difference in coefficient of thermal expansion (CTE) between the substrate and the subsequent layer. For GaN-based devices, three types of substrates are used, namely sapphire, SiC, and Si, and Tab. 2.1 shows an overview of the relevant parameters of these materials in comparison to GaN. In this project AlGaN/GaN HEMTs with a substrate of Si(111) are used.

Table 2.1. Overview of key parameters of the substrate materials sapphire, SiC, and Si compared to GaN. Values adopted from [21].

	Sapphire	**SiC**	**Si**	**GaN**
Lattice mismatch (%)	14	3.5	17	-
CTE mismatch (%)	−26	25	56	-
Energy band gap (eV)	9.9	4H-SiC: 3.26 6H-SiC: 3.03	1.12	3.4
Thermal stability (relative)	Very high	Very high	Moderate	-

The lattice mismatch and difference in CTE between GaN and the substrate leads to the formation of threading dislocations (TDs) in the GaN layer with a density in the range of $10^8 - 10^{10}$ cm^{-2} [22]. The formation of TDs reduces stress, however, penetration of TDs through the 2DEG largely degrades the mobility of the electron gas due to scattering of electrons [21]. It has been observed that for HEMTs with a 2DEG density above 1×10^{13} cm^{-2}, the room temperature electron mobility was degraded with increased TD density of $> 1 \times 10^{10}$ cm^{-2} [23], and thus it is desirable to reduce the density of TDs as much as possible. Therefore, an AlN nucleation layer is introduced between the substrate and the GaN layer to accommodate the lattice mismatch and difference in CTE between those two [21]. When investigating the HEMTs, the density of TDs is often determined by the density of V-defects on the surface as it is found that the bottom of a V-defect is most likely connected to a TD [24]. The V-defects are open hexagonal, inverted pyramids and it is found that these are formed due to an increase in strain energy and a reduction of Ga on the $\{10\bar{1}\bar{1}\}$ side walls compared to the (0001) surface [24]. An illustration of TDs connected to the bottom of V-defects in an AlGaN/GaN HEMT is shown in Fig. 2.8.

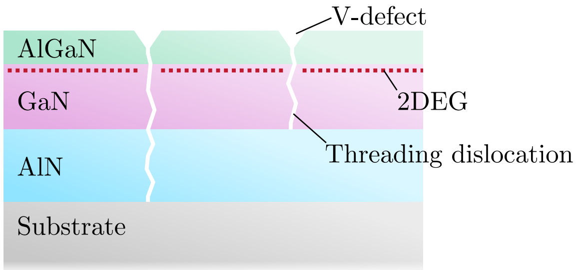

Figure 2.8. Illustration of the formation of TDs at the AlN/substrate and AlN/GaN interfaces due to lattice mismatch and difference in CTE. These TDs penetrate the 2DEG and are connected to the bottom of V-defects at the surface.

In [25] it was investigated how the growth conditions of an AlN buffer layer in an AlGaN/GaN heterostructure affected the quality of the device, here under the mobility of the 2DEG and the density of TDs. Four different AlGaN/GaN heterostructure samples were grown on sapphire substrates by metal organic vapour phase epitaxy (MOVPE), all having the same AlN nucleation layer. The subsequent AlN buffer layer of each sample were grown under various ammonia flux, leading to different thickness of this layer, measured by Rutherford back scattering (RBS) to be 700 to 800 nm for samples A and D and approximately 500 nm for samples B and C. Afterwards, a GaN layer, a nm thin AlN layer, three AlGaN barrier layers, and a GaN capping layer were grown in the same way for all four samples. High resolution atomic force microscopy (AFM) topography images at the size of 2×2 µm^2 were obtained. These high resolution images, as the one seen in Fig. 2.9, show pits which are located at the terrace joint points, thus being a clear indication that these pits can be associated with V-defects connected to TDs. From these high resolution images it is found that the surface density of V-defects is around 2×10^9 cm^{-2} for samples A and D and 4×10^9 cm^{-2} for samples B and C. These are comparable to a density of $\sim 5 \times 10^9$ cm^{-2} reported in [26] but an order of magnitude higher than a density of 4.16×10^8 cm^{-2} reported in [27]. This result shows that the density of TDs has been reduced by half in the samples having a thicker AlN buffer layer, as this increased thickness reduces stress caused by lattice mismatch between AlN and the sapphire substrate.

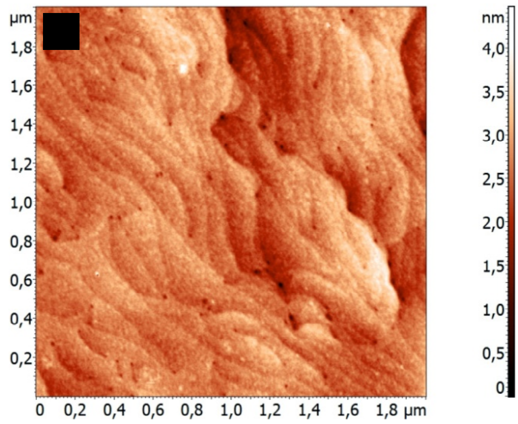

Figure 2.9. High resolution AFM topography images at the size of 2×2 µm^2 showing V-defects. Adopted from [25].

The electrical properties of the samples have been measured by Hall measurements in the van der Pauw configuration and the results are summarised in Tab. 2.2.

Table 2.2. Summary of sample sheet resistance, charge carrier concentration, and mobility of the four samples obtained by Hall measurements in the van der Pauw configuration. Values adopted from [25].

Sample	$\mathbf{R_s}$ **[Ω/sq.]**	$\mathbf{n_s}$ **[cm^{-2}]**	**µ [cm^2/V·s]**
A	541	1.02×10^{13}	1130
B	1030	0.97×10^{13}	622
C	800	1.07×10^{13}	730
D	474	1.14×10^{13}	1150

These results reveal similar charge carrier concentrations of approximately 1×10^{13} cm^{-2} for all four samples, which is comparable to the state-of-the-art values, while even the lowest sheet resistances of $474 - 541$ Ω/sq. are higher than the state-of-the-art values of $225 - 350$ Ω/sq. [26–31]. Considering the mobility, this is found to be highest for samples A and D with values of $1130 - 1150$ cm^2/V·s which are lower than the state-of-the-art values of $1400 - 2250$ cm^2/V·s [26–31] due to the relatively high density of TDs. In samples B and C, where the density of TDs is doubled, the mobility is reduced by a factor two. Thereby, these results clarify the necessity of improving the growth conditions of an AlN buffer layer in order to reduce the density of TDs and, as a consequence of this, increase the mobility of electrons in the HEMT.

The growth conditions of the AlN layer has also been of interest for Pan et al. in [32], where it was investigated how the growth temperature of the AlN layer affected the electronic properties of the HEMT. Here it was found that the density of TDs decreased for the growth temperature increasing to the optimal 1040°C. This revealed a charge carrier concentration of 1.026×10^{13} cm^{-2}, a sheet resistance of 313.2 Ω/sq., and an electron mobility of 1940 cm^2/V·s, all comparable to the state-of-the-art values [26–31].

The density of V-defects on AlGaN/GaN HEMTs has also been investigated in the previous semester project [20] on the samples on which the KPFM measurements shown in Fig. 2.7 were also obtained. In order to determine the number of V-defects per unit area, high resolution topography images at the size of 2×2 µm^2 were required. These were obtained for two samples having an AlGaN barrier layer thickness of $1-2$ nm and 10 nm, respectively, by AFM measurements with a sharp Si cantilever. The number of V-defects was determined using the software *ImageJ*, and each sample was scanned three times in order to find an average number of V-defects per unit area. A 2×2 µm^2 scan of the sample having an AlGaN barrier thickness of 10 nm is shown in Fig. 2.10. The grey scale image is included as it displays higher contrast and thus makes it easier to identify the V-defects.

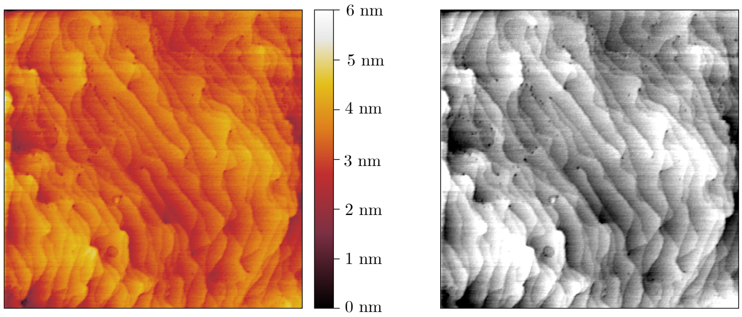

Figure 2.10. A 2×2 µm^2 AFM topography image of the sample having an AlGaN barrier layer thickness of 10 nm obtained with a sharp Si cantilever. The grey scale image displays higher contrast, making it easier to identify V-defects. Results from the previous semester project [20].

The average number of V-defects on the scans of the two samples as well as the calculated number of V-defects per cm^2 are shown in Tab. 2.3.

Table 2.3. Average number of V-defects per unit area calculated from three scans of samples having an AlGaN barrier layer thickness of $1-2$ nm and 10 nm, respectively. Results from the previous semester project [20].

AlGaN barrier layer thickness [nm]	Mean number of V-defects per 4 µm^2	Number of V-defects per cm^2
1-2	120.67 ± 10.66	3.02×10^9
10	121.33 ± 6.38	3.03×10^9

These results show a density of V-defects lying within the interval of the samples presented in [25], and thus the obtained densities seem reliable. Furthermore, it is observed that the density is the same for the two samples, in spite of the difference in the AlGaN barrier layer thickness. This is due to the AlGaN layer being very thin on both samples, and it is thus not able to relax and create TDs. Therefore, the observed V-defects are expected to originate from the underlying GaN and AlN layers, which are approximately the same for both samples.

2.3 Fabrication of Ohmic Contacts

When fabricating wide band gap semiconductors, such as GaN, an important matter to consider is the design of proper electrical contacts. As for all electronic devices, contacts provide the link between the device and external circuitry and vice versa, which means that they are critical for the functionality of the device. It is important that the contacts have a negligible resistance compared to that of the semiconductor drift layer, in order to minimise the on-resistance of the device and, hence, the power losses of the system [12]. It is also of great importance that the contacts are ohmic, meaning that they exhibit a linear current-voltage dependency, in order to eliminate a sudden drastic raise in resistance for a specific value of electrical current [10]. Electronic devices based on GaN requires a low specific contact resistivity, ρ_c, in values of 10^{-5} to $10^{-6}\,\Omega \cdot \mathrm{cm}^2$. However, obtaining good low resistance ohmic contacts for GaN is inherently difficult, as it has a band gap of 3.5 eV. This means that it will typically lead to a Schottky barrier height in the order of 1 eV for *n*-type, 2 eV for *p*-type, and even higher values for the case of $Al_xGa_{1-x}N$ alloys where the band gap increases with an increasing concentration of Al [12]. The difference in voltage-current dependency for ohmic contacts and Schottky barriers is illustrated in Fig. 2.11.

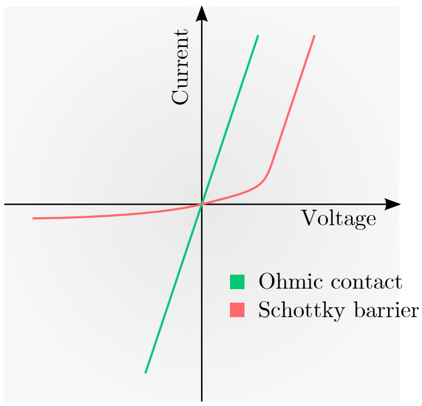

Figure 2.11. Sketch of voltage-current characteristics of ohmic contacts and Schottky barriers.

From this figure it is seen that a Schottky barrier requires a higher voltage to obtain the same current as for an ohmic contact. As production of such ideal contacts is critical for the functionality of GaN-based devices, this section will include a variety of solutions for fabrication of proper low resistance ohmic contacts. To establish a foundation for understanding these solutions, general physics revolving ohmic contacts will also be covered.

2.3.1 Essential Physics and Problematics of Ohmic Contacts

An ohmic metal/semiconductor contact is defined by two criteria. Firstly, as previously mentioned, it must exhibit a linear or quasi-linear current-voltage characteristic [11]. Secondly, the potential barrier at the metal/semiconductor interface must be absent or thin enough to allow for carrier tunnelling [12].

An important parameter for characterisation of ohmic contacts is the contact resistance, R_c, normally given in units of Ω. It is defined as the total resistance of the metal/semiconductor interface. As for the resistance of an ordinary resistor which is dependent on its own dimensions, the contact resistance depends on the size of the contact area. To avoid this dimension influence a more robust size is introduced, namely the specific contact resistivity, ρ_c, which is an analogy to the resistivity of an ordinary resistor. It is typically expressed in units of $\Omega \cdot \mathrm{cm}^2$ and can mathematically be defined as

$$\rho_c = \left.\frac{\partial V}{\partial j}\right|_{V=0}, \tag{2.12}$$

where j is the current density and V is the applied voltage [10–12]. The specific contact resistivity is dependent on the height of the Schottky barrier, ϕ_B, at the metal/semiconductor interface and on the doping level of the semiconductor, N_D. Utilising the Schottky-Mott theory, the height of the Schottky barrier, which is formed upon electrical contact, can be calculated using the work function of the metal, ϕ_m, and the electron affinity of the semiconductor, χ, which both are visualised in Fig. 2.12.

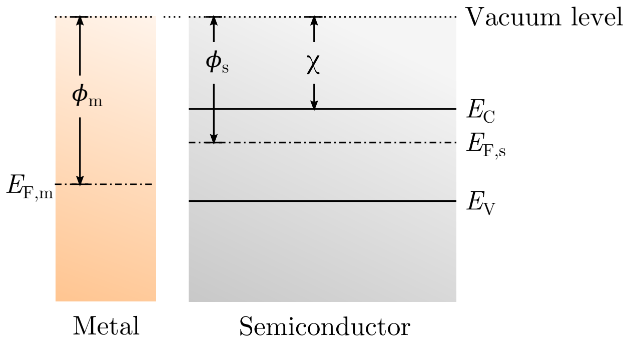

Figure 2.12. Illustration of the energy levels of a metal and semiconductor that are not electrically connected.

The relation describing the height of the Schottky barrier can for the case of an *n*-type semiconductor be written as [11, 12]

$$q\phi_B = q\phi_m - \chi. \tag{2.13}$$

Likewise, for the case of a *p*-type semiconductor, it can be written as [12]

$$q\phi_B = E_g - (q\phi_m - \chi), \tag{2.14}$$

where E_g is the difference in energy between the minimum of the conduction band, E_C, and the maximum of the valence band, E_V, and is typically referred to as the band gap. By considering these two equations, it is seen that the Schottky-Mott theory states that the height of the barrier, using a specific semiconductor, can be adjusted merely by choosing a metal with appropriate work function. Overall there are three types of possible barriers, namely the cases where $\phi_{\mathrm{m}} > \chi$, $\phi_{\mathrm{m}} = \chi$, and $\phi_{\mathrm{m}} < \chi$, which are called accumulation, neutral, and depletion, respectively. These names describe the behaviour of charge carriers near the interface, and the three cases are illustrated for an n-type semiconductor in Fig. 2.13.

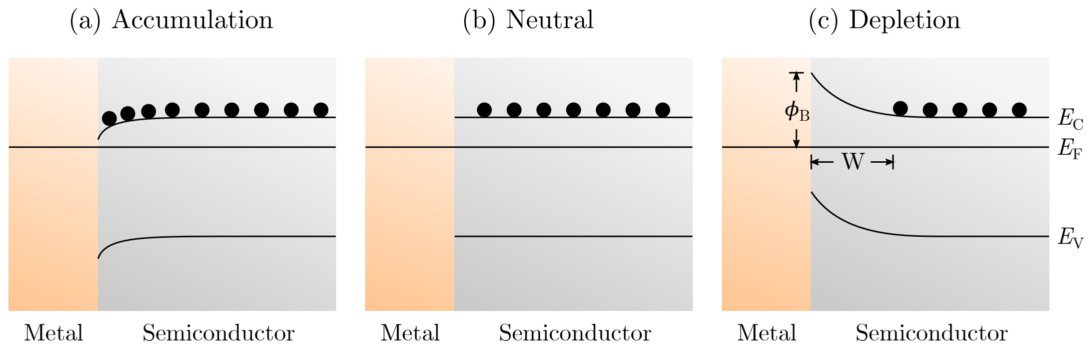

Figure 2.13. Mechanisms of carrier transport at a metal/semiconductor interface, described by the Schottky-Mott model. For the case of depletion, the height of the Schottky barrier, ϕ_{B}, and the width of the space charge region, W, has been illustrated.

From this figure it is obvious that the favourable type of ohmic contact would be of the accumulation-type as the charge carriers here encounter the lowest barrier flowing in or out of the semiconductor. However, for common semiconductors such as Ge, Si, and GaAs it has been experimentally observed that the barrier height is somewhat independent on the work function of the metal, which results in accumulation-type contacts being difficult to engineer [11], even though these semiconductors have a relatively small band gap and low electron affinity. Generally, depletion-type contacts are formed on both n- and p-type of these common semiconductor substrates creating high potential barriers [11], hence it is necessary to consider other solutions for creating proper ohmic contacts.

However, for the case of GaN, which has a wide band gap, the height of the potential barrier is well predicted by the Schottky-Mott Theory, and can thus be described by Eqs. (2.13) and (2.14). Therefore, the specific contact resistivity of contacts on n-type GaN can be decreased by choosing a metal with a low work function, whereas for a p-type GaN it can be decreased by choosing a metal with a high work function. The height of the Schottky barrier as a function of the metal work function has been summarised by [12] for different metals on n- and p-type GaN, and is shown in Fig. 2.14.

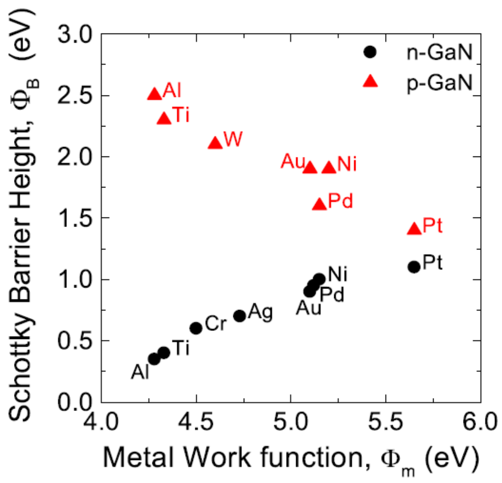

Figure 2.14. Measurements of Schottky barrier height as a function of metal work function for different metals on *n*- and *p*-type GaN. Adopted from [12].

As can be seen, the best options for contact materials on *n*-type GaN would be Al and Ti which result in a barrier height of 0.4 to 0.5 eV. For *p*-type GaN, however, it is much more difficult to decrease the barrier to a proper height since this would require metals with work functions over 6 eV. From Fig. 2.14 it can be seen that the best options for contact materials on *p*-type GaN would be Pt and Pd which result in a barrier height of around 1.6 eV. However, the focus of this project is on devices where electrons are the main charge carriers, thus the problematics regarding fabrication of ohmic contacts on *p*-type GaN will not be discussed further. Even though Al and Ti have relatively low work functions, single metal layers of Al or Ti are typically not suitable for ohmic contacts in GaN-based devices. This is partially due to the high propensity of oxidation for these materials, making them especially disadvantageous for high power applications where high temperatures are inevitable [12]. Furthermore, the use of a Ti single layer results in the formation of voids at the interface upon annealing, resulting in a bad mechanical contact. A solution to overcome these problematics is to use a stacking of metal layers, including a Ti/Al bilayer, which will adopt the advantageous physical properties of Al and Ti, but also eliminate some of the flaws. The proper designs of such metal stacking ohmic contacts will be discussed in the following section.

Another method for further lowering of the specific contact resistivity for *n*-type GaN is to increase the doping concentration directly under the contacts. By doing so, the energy of the conduction band drops such that the space charge region becomes sufficiently thin for electrons to tunnel through. This principle is illustrated in Fig. 2.15.

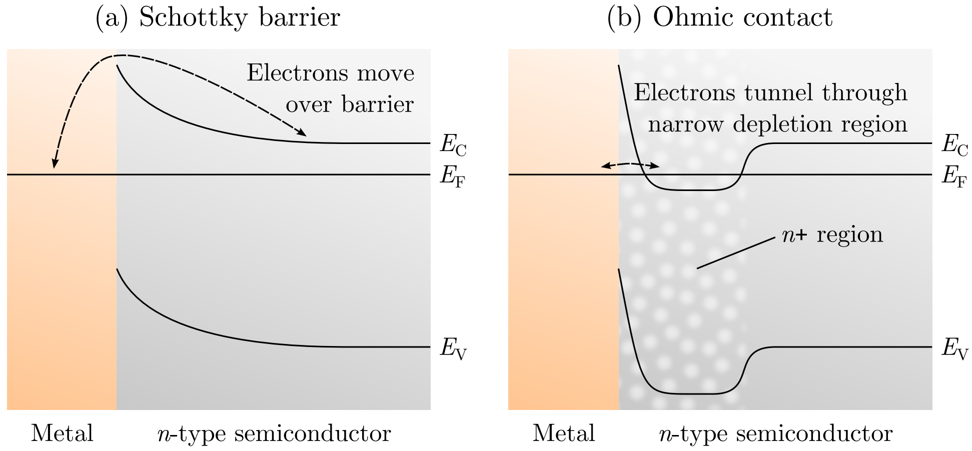

Figure 2.15. Band diagrams of a metal and n-type semiconductor in electrical contact. Here, (a) represents the scenario of a Schottky barrier, whereas (b) represents an ohmic contact where the part of the semiconductor closest to the metal has been additionally doped.

However, this technique is typically not used for AlGaN/GaN heterostructures, since intentional doping of the AlGaN barrier layer results in increased scattering of electrons in the 2DEG and, therefore, a lower electron mobility [12].

2.3.2 Ohmic Contacts on AlGaN/GaN Heterostructures

Fabrication of ohmic contacts on AlGaN/GaN heterostructures is inherently more difficult than on n-type GaN due to the wider band gap of AlGaN, which depends on the Al-content as described in Eq. (2.1). This wider band gap decreases the electron affinity, and hence increases the height of the Shottky barrier. One of the most widespread solutions for fabricating ohmic contacts on AlGaN, or n-type GaN in general, is to use a stacking sequence of specific metal layers as shown in Fig. 2.16.

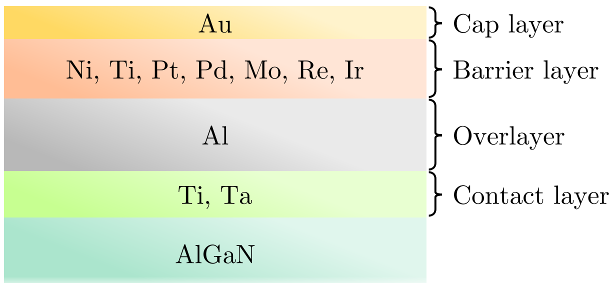

Figure 2.16. A metal stacking ohmic contact on an AlGaN/GaN sample. The names of each layers and the materials commonly used are stated in the figure.

In this stacking configuration each layer must have a negligible resistance, but besides this each of them also have a specific purpose. The contact layer, which is in direct contact with the AlGaN, must obviously have a low work function in order to decrease the height of the Shottky barrier as much as possible. Additionally, it also acts as a protection to limit diffusion of the upper layers into the AlGaN. Refractory metals such as Ti and Ta are typically used since they react with AlGaN to form the nitrate compounds TiN and TaN [12]. The formation of TiN leads to out-diffusion of N-atoms from AlGaN, which results in the formation of N-vacancies. These vacancies act as donors and, therefore, increase the carrier concentration below the TiN/AlGaN interface [12] which results in an energy configuration similar to the one shown in Fig. 2.15(b). However, as mentioned earlier, the formation of TiN can lead to voids below the TiN layer which makes the contacts mechanically weak. The amount of voids can be reduced using a higher content of Al for the AlGaN barrier since the formation of AlN is thermodynamically favourable compared to TiN, and hence a reduced amount of TiN is formed. Besides affecting the functionality of the ohmic contacts, the content of Al also affects the electron concentration of the 2DEG. Consequently, there are positive and negative effects from using a certain Al-content and, therefore, it has to be balanced properly. The purpose of the overlayer is to form low work function compounds with the surrounding metal layers, and thus Al is typically used [12]. The barrier layer acts as a protection for the other layers during annealing and, thus, typically consists of a material with a high melting point ($> 1400°C$). It limits diffusion between the over-/contact bilayer and the cap layer, and generally stabilises the multilayer structure during annealing [12]. Finally, the cap layer acts as a protective layer to avoid oxidation of the underlying layers, hence Au is often used. It is also of great importance that the cap layer is able to form a strong mechanical and electrical connection to an electrode [12].

Other aspects to consider when fabricating stacking ohmic contacts is the annealing temperature and layer thickness of the different metals. In most of the literature Ti and Al are used for the contact- and overlayer, respectively. Especially the thickness ratio between the contact- and overlayer, in this case Ti and Al, plays an important role in reduction of the specific contact resistivity [12]. In [12] the contact resistance for Ti/Al/Ni/Au stacking ohmic contacts is reported. Here, the thicknesses of Al, Ni, and Au are fixed at 200 nm, 50 nm, and 20 nm, respectively, whereas the thickness of Ti is varied to adjust the ratio of Ti/Al. The reported results are shown in Fig. 2.17 for different annealing temperatures.

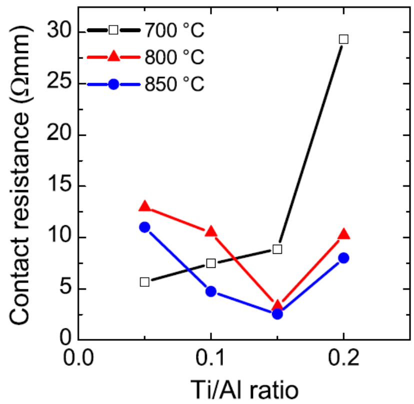

Figure 2.17. Contact resistance as a function of Ti/Al ratio for a Ti/Al/Ni/Au stacking ohmic contact on an AlGaN/GaN heterostructure. Multiple annealing temperatures were tested. Adopted from [12].

From these graphs it is seen that the lowest contact resistance for this stacking configuration occurs for a Ti/Al ratio of 0.15 at annealing temperatures of 800 and 850°C. However, this ratio varies depending on the choice of over-, barrier-, and cap layer thicknesses and materials as well as on the annealing temperature, annealing time, annealing condition, AlGaN barrier layer thickness, and Al-content of the AlGaN barrier layer. Thus, many parameters affect the specific contact resistivity, varying from 10^{-7} to 10^{-4} $\Omega\,\mathrm{cm}^2$ across the literature [12]. Some of the lowest specific contact resistivities found in literature are shown in Tab. 2.4 along with relevant information regarding the ohmic contacts and samples.

Table 2.4. Overview of some of the best stacking ohmic contacts on AlGaN/GaN heterostructures found in the literature. Partly adopted from [12].

Reference	**Layers (thicknesses)**	**AlGaN thickness**	**Al-content**	**Annealing conditions**	$\boldsymbol{\rho_c}$ **[$\Omega\,\mathrm{cm}^2$]**
[33, 34]	Ti/Al/Mo/Au (15/60/35/50 nm)	21 nm	0.28	850°C for 30 s in N_2	2.96×10^{-7}
[35]	Ti/Al/Ni/Au (20/120/55/45 nm)	22 nm	0.215	870°C for 50 s in N_2	9.6×10^{-7}
[36]	Ti/Al/Ni/Au (30/180/40/150 nm)	18 nm	0.25	900°C for 30 s in N_2	7.3×10^{-7}

From the methods and results presented in this section it is clear that construction and optimisation of ohmic contacts on AlGaN/GaN heterostructures is inherently complicated and depends on numerous factors.

Even more methods to improve the contacts are presented in the literature. An example of such method is to recess the contacts into the samples using chemical etching, in order to have a closer proximity between the 2DEG and the contacts, thus lowering the specific contact resistivity [37]. However, this method is out of reach for this project and will not be discussed further.

Chapter 3

Plasma Wave Theory

The 2DEG channel of a HEMT functions as a medium where oscillations in electron density, also known as plasma waves, can propagate in time and space and arise from reflections from the device boundaries. Under the right conditions, the oscillating electric field generated from the plasma waves can result in coherent electromagnetic radiation, and vice versa. Hence, by constructing a HEMT of appropriate size and geometry a coupling between the 2DEG and radiation of a specific range of the electromagnetic spectrum can be achieved. The range of interest for this project is the THz gap which spans from 0.1 to 10 THz [38]. Research has shown a great potential for the use of HEMTs as emitters, detectors, and modulators of THz radiation [5], resulting in a new and growing area of research. The focus of this project is amplitude modulation of THz radiation by the use of AlGaN/GaN HEMTs with resonant frequencies lying in the THz range. Therefore, it is necessary to introduce plasma wave theory considering the instability of the 2DEG in a short channel HEMT, also known as the Dyakonov-Shur instability.

This chapter will consider the theory describing the growth of plasma waves in a FET on the submicron scale with a 2DEG channel, which is the key to understanding the workings of a THz HEMT device. Plasma waves in the 2DEG will appear as an instability in the electron flow. From this consideration it will emerge that in a ballistic FET, where there are no collisions of electrons with phonons or impurities but many electron-electron collisions due to the high electron density, the 2DEG will show hydrodynamic behaviour like that of shallow water [6, 7]. Before making the shallow water analogy, the dispersion relation for plasma waves in a FET channel will be introduced.

3.1 Dispersion Relations for Plasma Waves in a FET

The dispersion relation for plasma waves depends on the dimension of the problem and whether the region of the electron gas is gated or ungated. However, it can all be derived by neglecting collisions and considering the average drift velocity, $\mathbf{v}$. Then, the small signal equation of motion and the continuity equation are given as

$$\frac{\partial \mathbf{j}}{\partial t} = \mathbf{E}\frac{e^2 n_\mathrm{s}}{m} \tag{3.1}$$

and

$$\frac{\partial \rho}{\partial t} + \operatorname{div} \mathbf{j} = 0, \tag{3.2}$$

respectively, where Eq. (3.1) is obtained from Newton's second law of motion by neglecting electron scattering. Here $\mathbf{j} = en_{\mathrm{s}}\mathbf{v}$ is the current density, m is the effective mass of electrons, $\mathbf{E}$ is the small signal electric field, and ρ is the small signal charge density which is related to the deviation of n_{s} from its equilibrium [6, 39]. In order to obtain the three dimensional bulk plasma frequency, Eq. (3.2) is differentiated with respect to time. Thus, by inserting Eq. (3.1), it is obtained that

$$\frac{\partial^2 \rho}{\partial t^2} + \frac{e^2 n_{\mathrm{s}}}{m} \operatorname{div} \mathbf{E} = 0. \tag{3.3}$$

The well-known relation between $\mathbf{E}$ and ρ is given from Gauss' Law as

$$\operatorname{div} \mathbf{E} = \frac{\rho}{\varepsilon}, \tag{3.4}$$

where ε is the dielectric permittivity. Substituting this into Eq. (3.3) yields a harmonic oscillator equation, and thus the three dimensional bulk plasma frequency is found to be the well-known expression [6, 39]

$$\omega_p = \sqrt{\frac{e^2 n_{\mathrm{s}}}{\varepsilon m}}. \tag{3.5}$$

Considering a gated 2DEG in a FET, the electron sheet concentration in the channel is related to the electric potential difference between the gate and channel by

$$en_{\mathrm{s}} = CU, \tag{3.6}$$

corresponding to Eq. (2.5), where $C = \varepsilon/d$ is the gate-to-channel capacitance pr. unit area and d is the distance between gate and channel. Furthermore, $U = U_{\mathrm{g}} - U_{\mathrm{c}} - U_{\mathrm{th}}$, where $U_{\mathrm{g}} - U_{\mathrm{c}}$ is the potential difference between the gate and channel and U_{th} is the threshold voltage. It must be noted that Eq. (3.6) is only valid under the gradual channel approximation [6, 39]. Thus, applying that $\mathbf{E} = -\nabla U$, it follows from Eq. (3.6) that the relation between the in-plane electric field and charge density is given by

$$\mathbf{E} = -\frac{1}{C} \nabla \rho. \tag{3.7}$$

The relation in Eq. (3.7) can now be substituted into Eq. (3.3), and thus the two-dimensional wave equation for ρ is obtained as

$$\frac{\partial^2 \rho}{\partial t^2} - s^2 \nabla^2 \rho = 0, \tag{3.8}$$

where

$$s = \sqrt{\frac{e^2 n_{\mathrm{s}} d}{\varepsilon m}} \tag{3.9}$$

is the plasma wave velocity. The solutions to Eq. (3.8) are waves having a linear dispersion relation,

$$\omega = sk, \tag{3.10}$$

where ω and k are the plasma wave frequency and wave vector, respectively [6, 7, 39]. Using Eq. (3.6) and the expression of the gate-to-channel capacitance, the surface plasma wave velocity can also be stated by the gate voltage swing as

$$s = \sqrt{\frac{eU}{m}}. \tag{3.11}$$

Considering the ungated 2DEG, the dispersion relation can be obtained in a similar manner, and is found to be [6, 39]

$$\omega = \sqrt{\frac{e^2 n_s}{2m\varepsilon} k}. \tag{3.12}$$

The equations for the gated 2DEG are only valid in the limit were $kd \ll 1$, meaning that the distance between the gate and channel must be small compared to the wavelength of the plasma wave. In the case where $kd \gg 1$ it is not relevant to consider the gate, and the equations for the ungated 2DEG are instead obtained [6, 39].

3.2 Shallow Water Analogy

In a typical 2DEG the electron concentration is on the order of $n_s \approx 10^{12}$ cm^{-2} meaning an average distance between electrons, and hence a mean free path for electron-electron collisions, of approximately 100 Å. This condition makes the 2DEG both significantly non-ideal and non-degenerate. This means that the electron gas behaves like a fluid and thus the movement in the channel can be described by hydrodynamic equations from which the analogy to shallow water will appear [7].

The equation of motion of the electron fluid, known as the Euler equation, is given as

$$\frac{\partial v}{\partial t} + v\frac{\partial v}{\partial x} + \frac{e}{m}\frac{\partial U}{\partial x} + \frac{v}{\tau} = 0, \tag{3.13}$$

where $\partial U/\partial x$ is the longitudinal electric field in the channel, $v(x,t)$ is the local velocity of electrons, and τ is the momentum relaxation time. Here, the last term accounts for collisions of electrons with phonons or impurities and, furthermore, viscosity of the electron fluid has been neglected [6, 7]. Eq. (3.13) must be solved together with the usual continuity equation

$$\frac{\partial n_s}{\partial t} + \frac{\partial (n_s v)}{\partial x} = 0, \tag{3.14}$$

which, using Eq. (3.6), can also be written as

$$\frac{\partial U}{\partial t} + \frac{\partial (Uv)}{\partial x} = 0. \tag{3.15}$$

It now emerges that Eqs. (3.13) and (3.15) coincide with the hydrodynamic equations of shallow water, thus making it clear that the two-dimensional electron fluid behaves like shallow water. In this analogy v corresponds to the fluid velocity, and eU/m corresponds to gh, where h is the level of the shallow water and g is the free-fall acceleration [6, 7, 39]. Assume that the swing voltage is fixed at a value U_0 and zero channel current. The dispersion relation obtained from the linearised system of Eqs. (3.13) and (3.15) is thus

$k = \pm\omega/s$, which is exactly the dispersion relation for shallow water, where $s = (eU_0/m)^{1/2}$ is the plasma wave velocity [6, 7]. When the velocity of the electrons in the FET channel is v_0 the dispersion relation becomes $k = \pm\omega/(v_0 \pm s)$, thus showing that the plasma waves are carried along by the electron flow [6, 7].

It is now time to set up some boundary conditions by considering the case where the source and gate are connected to a voltage source, U_{gs}, and the source and drain are connected to a current source. Thus there is a constant gate-to-source voltage $U = U_0$ at the source, $x = 0$, and a constant current at the drain, $x = L$. The source is short circuited to the gate by the voltage source, thus making it possible to have AC current at the source, even in the case of a constant external current. These boundary conditions correspond to having zero impedance at the source and infinite impedance at the drain, meaning a short circuit at the source side of the channel and an open circuit at the drain side of the channel [7].

Considering the velocity of the plasma waves this is different for the two propagation directions, and this difference will create an instability in the electron flow. In order to show this, Eqs. (3.13) and (3.15) are linearised by $v = v_0 + v_1 \exp(-i\omega t)$ and $U = U_0 + U_1 \exp(-i\omega t)$ with respect to v_1 and U_1, which are small variations of U and v around their steady state values. Furthermore, the boundary conditions used are $U_1(0) = 0$ and $\Delta j(L) = 0$, as has been discussed earlier [6, 7]. The solution to this is the sum of two waves, one propagating from the source to the drain and one propagating from the drain to the source, and is thus of the form

$$v_1 = A\exp(ik_1x) + B\exp(ik_2x) \tag{3.16}$$

$$U_1 = C\exp(ik_1x) + D\exp(ik_2x). \tag{3.17}$$

The wave vectors, k_1 and k_2, are given as

$$k_1 = \frac{\omega}{s_1} = \frac{\omega}{s + v_0} \tag{3.18}$$

$$k_2 = \frac{\omega}{s_2} = \frac{\omega}{s - v_0} \tag{3.19}$$

and thus they incorporate the different velocities in each direction [6, 7]. From this approach it is found that the real and imaginary parts of the plasma wave frequency, $\omega = \omega' + i\omega''$, are given as

$$\omega' = \frac{|s^2 - v_0^2|}{2Ls}\pi n \tag{3.20}$$

$$\omega'' = \frac{|s^2 - v_0^2|}{2Ls} \ln\left|\frac{s + v_0}{s - v_0}\right|, \tag{3.21}$$

where n is an odd integer for $|v_0| < s$ and an even integer for $|v_0| > s$ [6, 7]. Thus, in the case where $v \ll s$ the plasma wave frequency is given as the odd harmonics of the fundamental plasma frequency [8, 40]

$$\omega_0 = \frac{\pi s}{2L}. \tag{3.22}$$

Eq. (3.21) is the wave increment in units of $s/2L$ which only depends on the Mach number, $M = v_0/s$. In Fig. 3.1 the dimensionless increment, $2\omega''L/s$, is plotted against $M = v_0/s$.

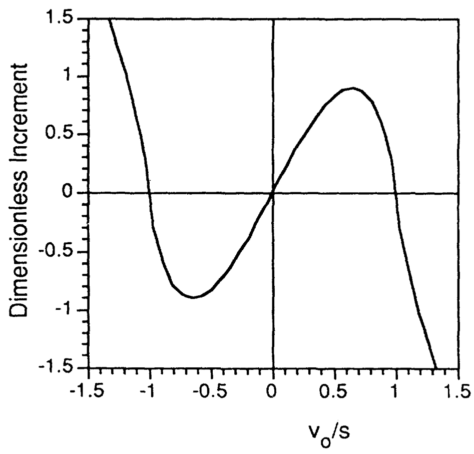

Figure 3.1. Dimensionless increment of plasma wave, $2\omega'' L/s$, as a function of $M = v_0/s$, called the Mach number. From this illustration it is clear that the electron flow is unstable in the regions of $0 < v_0 < s$ and $v_0 < -s$. Adopted from [7].

Eq. (3.21) together with Fig. 3.1 clarifies that when v_0 is positive, the steady flow of electrons is stable when $v_0 > s$ and unstable when $v_0 < s$. In the opposite case where v_0 is negative, meaning interchanging the boundary conditions at the source and drain, the steady flow is stable when $|v_0| < s$ and unstable when $|v_0| > s$. In the case where $M \ll 1$ the wave increment becomes $\omega'' = v_0/L$, which is recognised as the inverse electron transit time [6, 7, 39]. The most important case for the purpose of practical use is $s > v_0 > 0$, where the steady flow of electrons is unstable at low electron velocities, v_0. This instability is related to the reflection of the plasma waves from the device boundaries. From the solution of the linearised Eqs. (3.13) and (3.15) it follows that at $x = 0$, where the voltage is constant, there is no change in the wave amplitude. However, at $x = L$, where the current is held constant, the ratio of the amplitudes of the reflected and incoming waves is $(s + v_0)/(s - v_0)$, thus confirming that the plasma wave amplitude increases when $v_0 < s$ [7].

Next, let $\tau = L/(s + v_0) + L/(s - v_0)$ be the time it takes for the wave to travel from the source to the drain and back. During each reflection from the drain the amplitude grows and thus, during the time t, the wave amplitude will increase by $[(s + v_0)/(s - v_0)]^{t/\tau}$, where t/τ is the number of rounds the wave have travelled in the time t. Eq. (3.21) is thus obtained by equating $[(s + v_0)/(s - v_0)]^{t/\tau}$ to $\exp(\omega'' t)$. From this it emerges that the growth of plasma waves occurs during the reflection of the wave from the device boundary where the current is held constant [7].

There are primarily two mechanisms which may oppose the growth of these plasma waves. The first decay mechanism is external friction occurring from electron collisions with impurities and phonons, which are not present when considering a ballistic FET. This can be accounted for by retaining the last term, v/τ, of Eq. (3.13). In this case the term $-1/2\tau$ will be added to the wave increment, meaning that the wave will only grow when the number of collisions during the electron transit time is small. The second decay mechanism is internal friction occurring from the viscosity of the electron fluid. This is accounted for by a damping term in the wave increment of ηk^2, where η is the viscosity. The increment of the plasma wave must be compared to the decrement terms caused by both collisions and viscosity in order to find the threshold velocity of electrons for the increment to dominate. When the velocity of electrons exceeds this threshold velocity the plasma waves will grow [6, 7].

Chapter 4

Review of THz Modulators

This chapter is a review of designs of the THz modulators presented in the literature, including split-ring resonators (SRRs), frequency selective surface structures (FSSs), and grating-gate HEMTs. This will work as the stepping stone towards choosing the designs of the THz modulators fabricated and measured upon in this project.

4.1 Split-Ring Resonators

In the search of devices, such as THz modulators, covering the terahertz gap the development of the technology has been limited by both the material of the substrate and the structure of the device [41]. However, it is found that these challenges can be overcome by the use of so-called metamaterials of specific structures. Metamaterials are composite artificial materials often known for the electronic property of negative refractive index. In [42] it is defined as an artificially structured material with properties obtained from the unit structure instead of the materials of which it consists. Furthermore, the length scale of features is much smaller than the relevant wavelength, making the material uniform on a large scale.

For the research of terahertz devices, such as modulators, an often used metamaterial structure is the split-ring resonator (SRR). In the literature several groups have researched terahertz modulators by devices consisting of an array of SRRs on top of an array of HEMTs. In the following the devices and results obtained in [5] and [41] with GaAs-based HEMTs will be considered.

In [5] a resonant frequency in the terahertz range was obtained using a device consisting of unit cells of metamaterial on GaAs-based HEMTs at the size of the metamaterial unit cells. These individual cells were connected in arrays within each row thus making one large device.

The sample consisted of a 100 µm semi-isolating GaAs substrate on top of which three metal layers, a GaAs-based HEMT, and an isolating encapsulating layer of silicon nitride was constructed. The top 2.1 µm layer of gold was deposited in a shape making it the metamaterial layer and, furthermore, another metal layer was deposited to form the gate. In order to connect the source and drain of the device to the HEMT, a 0.176 µm thick ohmic contact layer was deposited and, furthermore, the source and drain were shorted by the SRR design of the metamaterial. The design of this device is illustrated in Fig. 4.1.

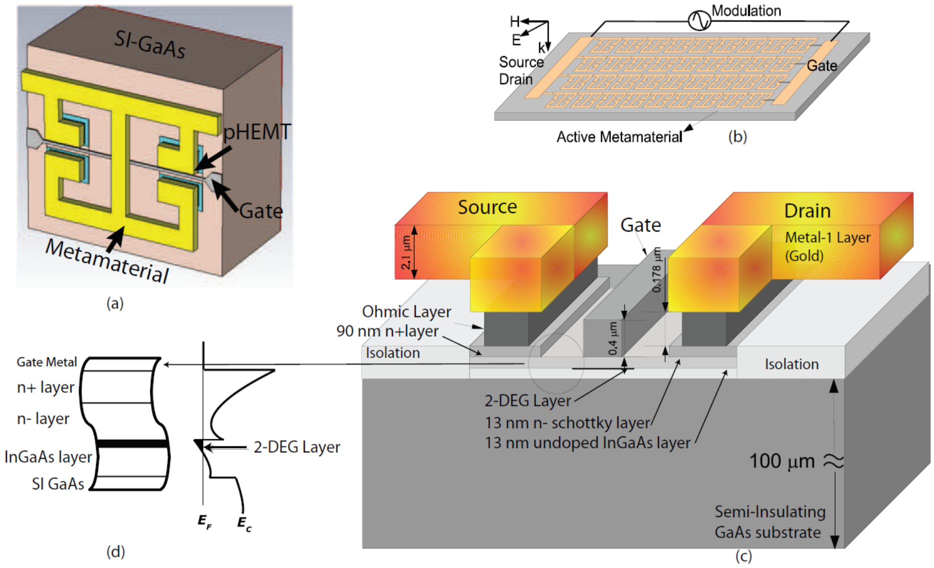

Figure 4.1. Details on a metamaterial/GaAs-based HEMT device with transistors at the size of the metamaterial unit cell. (a) Unit cell revealing an SRR geometry of the metamaterial. The HEMT is located underneath the split gap. (b) Illustration of the array of unit cells creating the total device including the polarisation orientation of the incoming THz wave. (c) Cross-section of the split gap revealing the individual layers of the structure. (d) Band diagram of the Schottky/InGaAs layer heterojunction revealing the formation of the 2DEG. Adopted from [5].

In Fig. 4.1(a) the geometry of the metamaterial is seen and reveals an SRR design. Each unit cell contains of two split-rings each having a split gap width of 3 µm and a line width of 4 µm. The metamaterials have a width of 42 µm and a height of 30 µm and are connected in an array with a period of 55×40 µm^2. This array is seen in Fig. 4.1(b) and consists of 3200 elements with a total size of 2.75×2.6 mm^2. The arrays are connected within each row through the gates to a single bond pad by wires of the same gate metal, thus providing the gate bias voltage. Likewise, the arrays are also connected within each row by the use of the same metal layer as for the metamaterial. At the perimeter of the device each row is connected vertically by the ohmic layer and all the individual elements are connected to another single bond pad which provides the bias voltage for the drain and source of the HEMT. The direction of the polarisation of the electric field is in the direction of the split gap, as this will drive the metamaterial SRRs into resonance [5]. Fig. 4.1(c) shows the details of the split gap of a single split-ring, and thus illustrates how the HEMT is located underneath the split gap. This HEMT consists of a 13 nm lightly doped Schottky layer and a 13 nm pseudomorphic undoped InGaAs layer. These layers create a heterojunction in which the 2DEG channel is formed. This is due to the conduction band bending below the Fermi energy, as explained in Sec. 2.1, and is seen in the band diagram in Fig. 4.1(d). This channel is even formed in the heterojunction of undoped layers with a high mobility of ~ 3000 cm^2/V·s and a charge density of $\sim 1.5 \times 10^{12}$ cm^{-2} at room temperature, thus making the channel a good conductor.

In order to understand the dependence between the source-drain current and the gate bias voltage this has been simulated and the result of this is shown if Fig. 4.2, where the drain-to-source current, I_{ds}, is shown as a function of gate bias, V_{gs}.

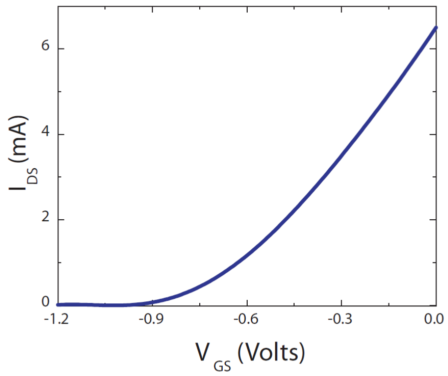

Figure 4.2. Simulation of I-V characteristics showing the drain-to-source current, I_{ds}, as a function of gate bias, V_{gs}. Adopted from [5].

From Fig. 4.2(a) it is expected that at a gate bias lower than −1.0 V, the 2DEG channel of the HEMT is completely depleted. As the gate bias increases towards 0.0 V the channel is formed.

The characterisation of the device was performed using a THz time-domain spectrometer (THz-TDS) with the electric field concentrated within the metamaterial split gap at the resonant frequency. For normalisation of the data a reference signal has been measured by removing the sample from the THz beam. The normalised results are shown in Fig. 4.3.

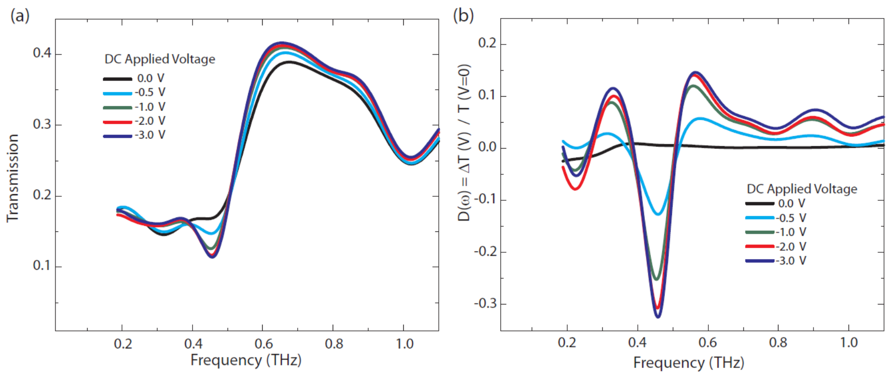

Figure 4.3. (a) Transmission for device as a function of frequency for varying gate bias. (b) Differential transmission as a function of frequency for varying gate bias. Adopted from [5].

Fig. 4.3(a) shows the transmission of the electric field as a function of frequency for gate biases between 0.0 V and −3.0 V. From the simulation in Fig. 4.2 it follows that the channel is completely depleted for gate biases below −1.0 V and the transmission results of lower gate biases reveal a resonant frequency of 0.46 THz. For gate biases above −1.0 V the channel begins to form, and so at 0.5 V the resonant weakens while at 0.0 V there is no resonance observed. Fig. 4.3(b) shows the differential transmission that as a function of frequency for different gate biases can be defined as

$$D(\omega) = \frac{T(\omega)_{V_{\mathrm{gs}}} - T(\omega)_{V_{\mathrm{gs}}=0\ \mathrm{V}}}{T(\omega)_{V_{\mathrm{gs}}=0\ \mathrm{V}}}. \tag{4.1}$$

Thus, this shows how the amplitude of the resonance switches with applied gate bias. The black curve in Fig. 4.3(b) illustrates the frequency dependent noise and was obtained by dividing two successive measurements of transmission, both at 0.0 V, by each other. Now, considering the measurement of a −0.5 V gate bias, there generally is a deviation of maximum 5% from the black curve, however, at the resonant frequency of 0.46 THz the deviation in differential transmission, known as the modulation depth, is −13 %. At the resonant frequency the transmission will continue to decrease with decreasing gate bias, and at a gate bias of −3.0 V the modulation depth is −33%. Thus, in [5] it is succeeded to manufacture a device consisting of arrays of SRRs revealing a resonant frequency of 0.46 THz with a differential transmission which is dependent on the applied gate bias.

In [41] a very similar approach and result was obtained. Here a THz modulator device was also manufactured by an array of SRRs on top of an array of GaAs-based HEMTs as shown in Fig. 4.4(a).

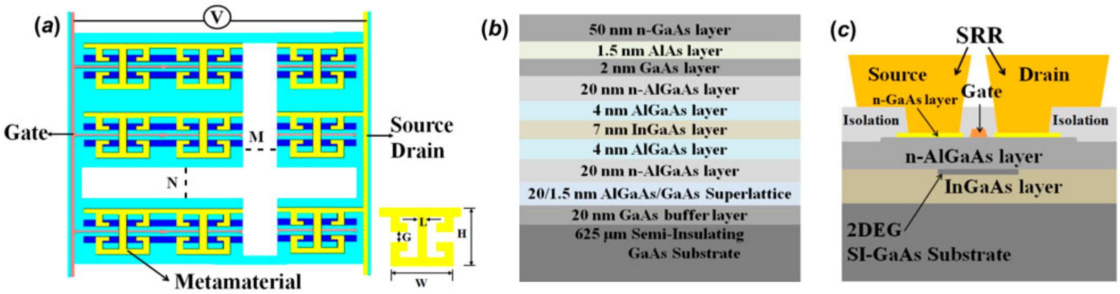

Figure 4.4. Design details of device. (a) Top-view of SRR array on top of HEMT array making up the THz modulator. The inset in the bottom right corner is the SRR unit cell with L = 5 µm, G = 5 µm, H = 30 µm, and W = 42 µm. (b) Layer structure of HEMT grown by MBE. (c) Cross-section of a single element showing the ohmic contacts, gate, and location of 2DEG channel. Adopted from [41].

The GaAs-based HEMT was grown by molecular beam epitaxy (MBE) on a 635 µm thick semi-insulating GaAs substrate and the details of the individual layers are shown in Fig. 4.4(b). The 2DEG is located in the undoped InGaAs channel layer, and Hall measurements reveal a 2DEG density and electron mobility of 2.5×10^{12} cm^{-2} and 5000 cm^2/V·s, respectively. The ohmic contacts forming the source and drain were made from Ni/Ge/Au (15/40/150 nm) metal stacks while the Ti/Pt/Au (25/25/300 nm) metal stacks formed the gates. The SRRs were fabricated by electron beam evaporation (EBE) technology and photolithography and the SRR unit cell, shown in Fig. 4.4(a), is similar in design as the one of [5]. However, some small variations in the dimensions, along with possible deviations in the HEMTs, may give slightly different results. In [41] the SRR has both a line width, L, and split gap, G, of 5 µm. Each unit cell consists of two connected SRRs and thus the unit cell has a width, W, of 42 µm and a height, H, of 30 µm. Each element has a size of 55×40 µm^2, thus giving a total of $M \times N = 50 \times 64 = 3200$ elements and a total device size of 2.6×2.7 mm^2, similar to the device in [5]. Lastly, the gates all have a length of 1 µm and a width of 5 µm. The same metal stack forming the gates were used to connect the gates within each row to one large electrode on which it is possible to apply gate voltage. Similarly, the same metal stacks forming the ohmic contacts were used to connect all the SRRs in each row to one large electrode for the source and drain of the HEMT on which voltage can be applied.

The device was mounted on a 2×2 cm^2 printed circuit board with a 2.2×2.2 mm^2

square hole on which the THz beam was focused. The characterisation is performed using THz-TDS at room temperature, and the results can be seen in Fig. 4.5.

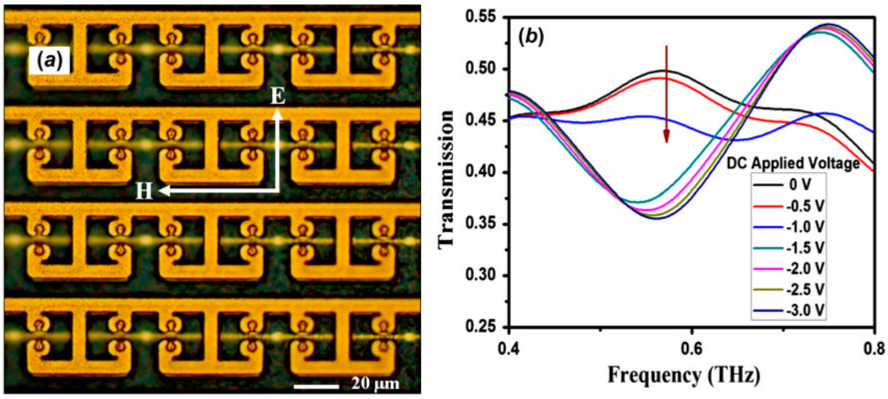

Figure 4.5. (a) Top-view of the array of SRRs which has been measured upon by the use of THz-TDS. (b) Results of transmission as a function of frequency for different applied gate biases between 0 V and −3.0 V. Adopted from [41].

As in [5] the data was normalised by a reference measurement performed by removing the sample from the THz beam. At a gate voltage of 0 V there is no resonance observed, as the 2DEG is fully formed underneath the split gap. When the gate bias is decreased to a voltage lower than −1.0 V the 2DEG begins to be depleted, and resonant behaviour can be observed. At −1.5 V a resonant frequency of 0.56 THz is thus observed. By further reduction of the gate bias to −3.0 V the transmission amplitude reduces to 0.35 at a resonant frequency which is slightly shifted to 0.58 THz, as can be observed in Fig. 4.5(b). This change in the transmission amplitude at −3.0 V compared to 0 V corresponds to a modulation depth of approximately −28%.

This comparison of results in [5] and [41] shows similar results with deviations which can clearly be attributed to the small variations in the dimensions of the otherwise similar designs. Furthermore, there can be deviations of the specific HEMTs used in the two experiments, which may affect the resonant frequency. However, the results show that even with these deviations in the dimensions the change in resonant frequency is still safely within the terahertz regime and does not vary drastically.

4.2 Frequency Selective Surface Structures

In this section the focus will be on [43] which is based on an AlGaN/GaN HEMT as the samples used for measurements in this project will be. In this work the modulators consisted of a frequency selective surface structure (FSS), which are periodic structures controlling the resonant frequency of the modulator by geometry, integrated on a single channel AlGaN/GaN HEMT with epilayers of GaN/$Al_{0.3}Ga_{0.7}N$/AlN/GaN (3/22/1/1300 nm) on a 450 μm sapphire substrate. Hall measurements of the formed 2DEG reveal an electron mobility and density of $\mu = 1800$ cm^2/V·s and $n_s = 4.4 \times 10^{12}$ cm^{-2}, respectively. Furthermore, the HEMT mesa has dimensions of $W \times L \times H = 38$ μm $\times$ 12 μm $\times$ 200 nm in width, length, and height, respectively, and the top electrodes consist of a 200 nm thick

Ni/Au stacking layer. The modulator, including the FSS structure and a unit cell image, is seen in Fig. 4.6.

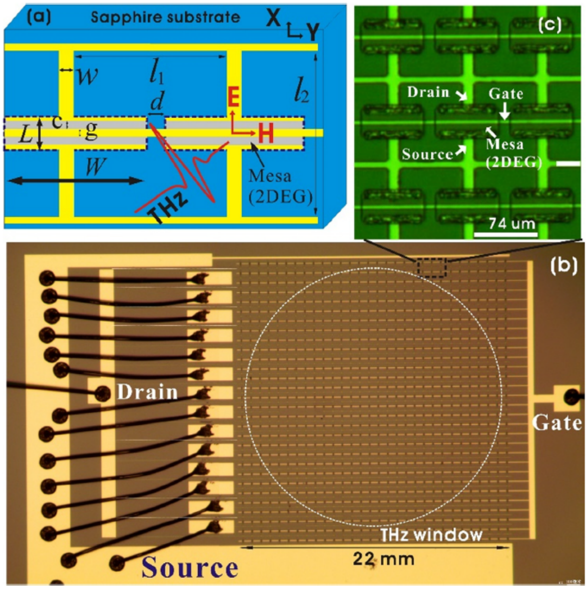

Figure 4.6. Illustrations of the THz modulator. (a) Schematic of the FSS structure. (b) Photo of the THz modulator showing the connection in arrays to larger source, drain, and gate electrodes. (c) Close-up of unit cells in the array. Adopted from [43].

Fig. 4.6(a) shows an illustration of the modulator unit cell, and the dimensions of the parameters given are l_1 = 28 µm, l_2 = 34 µm, c = 2.5 µm, g = 2 µm, d = 5 µm, and w = 4 µm. The incoming THz electromagnetic wave marked in the figure is propagating perpendicular to the surface of the modulator, and the electric field is in the x-direction. Fig. 4.6(b) shows an image of the entire modulator. Here it can be seen how the source, drain, and gate of the unit cells are connected within each row to larger separate source, drain, and gate electrodes thus making it possible to practically control the HEMT conductance by the applied gate bias, V_g. For measuring, the modulator was mounted on a copper sample holder with a hole through which the terahertz wave can pass and transmission could be measured. The active area of the modulator had dimensions of 2.2×2.2 mm^2, and with a focal spot of ∼ 2 mm^2 THz-TDS was used for the transmission characterisation.

The THz transmission was measured for different DC gate voltages and the result is shown in Fig. 4.7(a), where the transmission of the substrate has been subtracted from the transmission of the modulator.

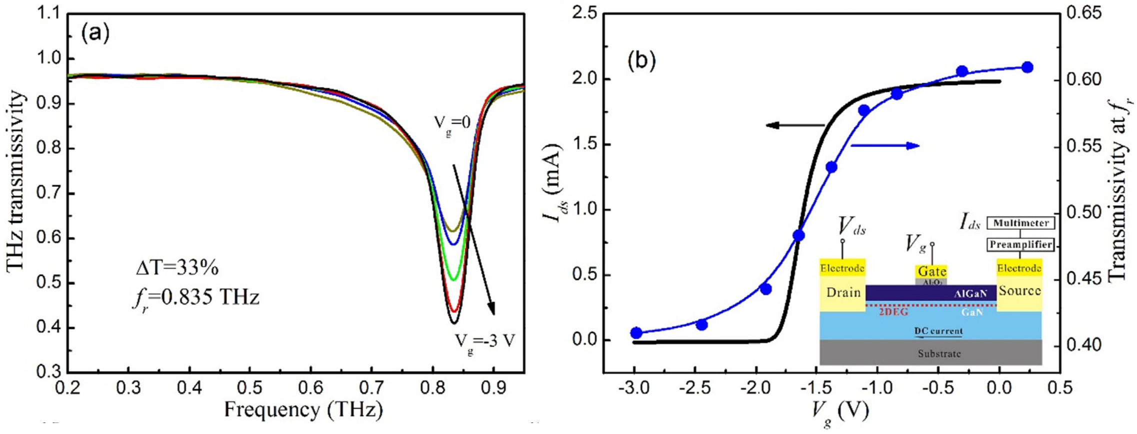

Figure 4.7. (a) THz transmission of the modulator as a function of frequency for different gate bias, V_g. (b) The black curve is the ***I-V*** characteristics of the modulator, where a small DC voltage of $V_g = 0.01$ V is applied to the drain while the source is grounded. The drain-to-source current is measured by a multimeter through a preamplifier, as shown in the inset. The blue curve is the transmission at the resonant frequency, f_r, for different V_g. Adopted from [43].

From these results it is observed that the resonant frequency of the modulator is $f_r = 0.835$ THz with the transmission decreasing from 0.61 at 0 V to 0.41 at −3 V, which gives a modulation depth of 33 %. In Fig. 4.7 the ***I-V*** characteristics of the HEMT is shown, obtained by applying a small drain-to-source DC voltage of $V_{ds} = 0.01$ V at the drain while grounding the source. The drain-to-source current, I_{ds}, is thus measured with a multimeter through a low-noise current preamplifier, as seen in the inset of Fig. 4.7(b). Considering the conductance of the HEMT it is observed that the electron channel is depleted at a gate bias of $V_g = -1.8$ V and, furthermore, a drastic change in conductance appears between a gate bias of −1.0 V and −2.0 V. This is also observed in the blue curve as a significant change in transmission at the resonant frequency, due to the depletion of the electron channel. Thus the results obtained in [43] reveal that it was possible to fabricate a THz modulator device on an AlGaN/GaN HEMT with a resonant frequency of 0.835 THz and modulation depth of 33 %.

4.3 Grating-Gate HEMT Structures

An alternative method for obtaining plasmon coupling with THz waves for the purpose of THz modulation is the use of grating-gate HEMTs. In these the plasma oscillation frequency differ depending on whether it is in the gated or ungated region and are given by Eq. (3.10) and Eq. (3.12), respectively. The reasoning of using a grating-gate instead of a single gate is that the gate is exhibiting large screening effects on the gate plasmons, and thus the plasmons are weakly coupled to the THz radiation. By the use of the large-area grating-gate it is expected to increase the plasmon coupling and improve the modulation properties [3].

In this section the focus will initially be on [3] where results of resonant frequency and THz modulation are obtained at room temperature in devices consisting of grating-gate structures of different periods on GaN-based HEMTs. Next, [44] will be included, as it is the results obtained by the same group when considering the dependence of temperature on resonant frequency for the same samples as were measured upon in [3].

An illustration of the design of the grating-gate device is shown in Fig. 4.8, where N_1 and N_2 are the 2D electron concentration in the gated and ungated region, respectively.

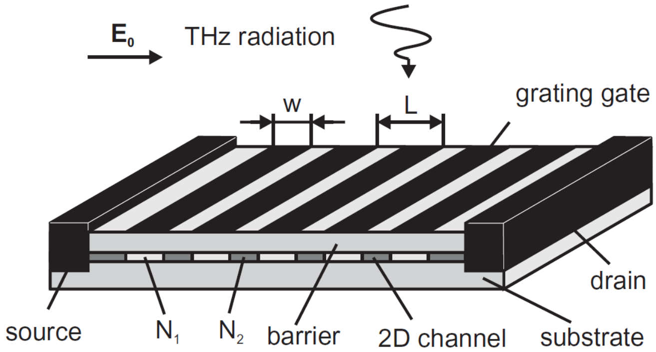

Figure 4.8. Illustration of large-area grating-gate device with a 2D electron channel. N_1 and N_2 are the electron concentration in the gated and ungated region of the channel, respectively. Adopted from [3].

The HEMT on which the grating-gate was integrated in the study of both [3] and [44] was an AlGaN/GaN heterostructure grown by metal-organic chemical vapour deposition (MOCVD) on a sapphire substrate. This heterostructure consisted of a 100 nm AlN buffer layer, a 1.4 µm undoped GaN layer, and an $Al_{0.2}Ga_{0.8}N$ barrier layer Si-doped to approximately 2×10^{18} cm^{-3}. Lastly, the source and drain ohmic contacts as well as the gate fingers were fabricated by e-beam evaporated Ti/Al/Au and Ni/Au metal stacks, respectively. Having introduced the device design as well as fabrication and materials the results of [3] and [44] will be presented separately.

In [3] the active region of the device had a size of 1.5×1.5 mm^2 which was covered by periodic grating-gate fingers of different length and spacing. The chosen gate lengths of the devices in this study were 1 µm, 2 µm, and 3 µm, while the chosen spacing between fingers were 0.5 µm and 1 µm. The transmission has been measured by a Fourier Transform Infrared (FTIR) spectrometer and the data was normalised by the measured transmission spectrum of the sapphire substrate. The result of the device with a gate length of 3 µm and 1 µm spacing is shown in Fig. 4.9, where the arrows indicate the theoretically expected resonant frequencies of the plasma waves for the first and second harmonics. Thus it is observed that the expected resonant frequencies correspond approximately to what is measured in the transmission spectrum.

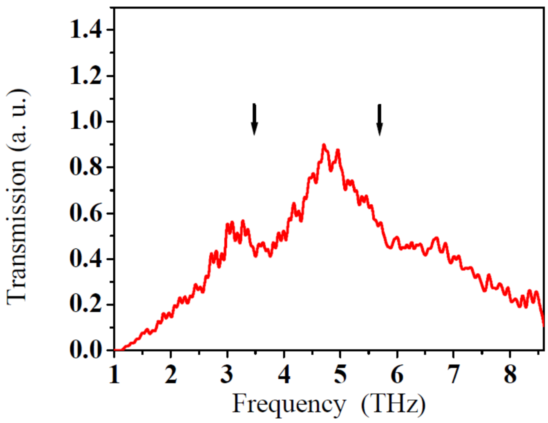

Figure 4.9. Measured transmission as a function of frequency for a sample with gate finger length of 3 µm and a gate finger spacing of 1 µm. The arrows indicate the theoretically expected resonant frequencies for the first and second harmonics. Adopted from [3].

Next, the modulation rate was investigated by measuring the transmission under several bias conditions using an optically pumped CW THz gas laser at different frequencies. Initially, the transmission amplitude of the THz beam through the grating-gate was measured at zero gate bias, and a mechanical chopper was used for modulating the THz beam at a frequency of 100 Hz. Next, the mechanical chopper was removed and a pulsed bias was applied to the grating-gate electrodes. The pulses had a duration and frequency of 5 ms and 100 Hz, respectively, while the amplitude varied between −8 V and 0 V and the intensity of the transmitted TH beam was measured by the pyroelectric detector. Fig. 4.10 shows the intensity of the transmitted THz signal and it is apparent that this follows the gate pulse, thus indicating a good modulation.

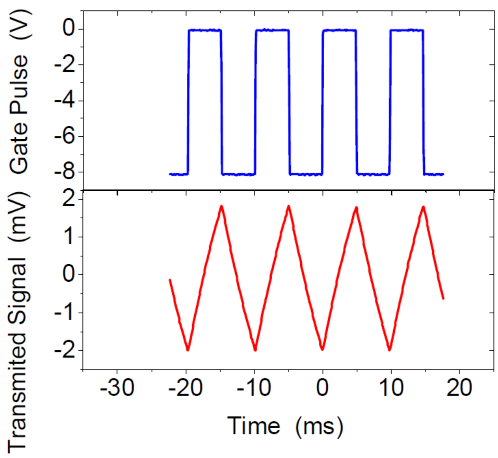

Figure 4.10. The upper curve shows the gate pulse varying between −8 V and 0 V. The lower curve shows the intensity of the transmitted THz signal. Adopted from [3].

The effective modulation rate is defined as

$$M = \frac{V_{\text{chopped}}}{V_{\text{pulsed}}}, \tag{4.2}$$

where V_{chopped} and V_{pulsed} are the signals measured by the pyroelectric detector under the conditions of modulation with and without the mechanical chopper, respectively. Fig. 4.11

shows the dependence of the modulation rate on the amplitude of the gate pulse for two different frequencies of 1.40 THz and 1.89 THz, respectively.

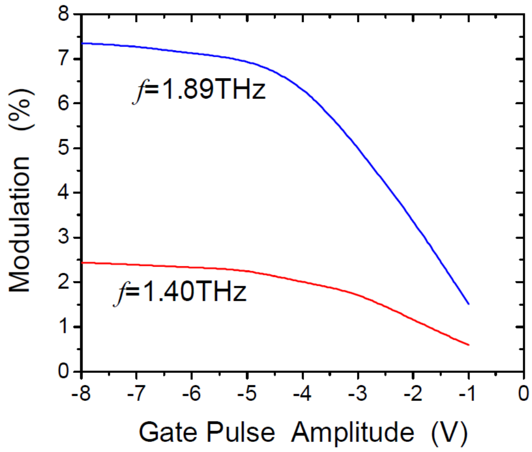

Figure 4.11. Effective modulation rate as a function of gate pulse amplitude for two different THz frequencies of 1.40 THz and 1.89 THz, respectively. Adopted from [3].

The device has a threshold voltage of $V_{\mathrm{th}} \approx -4.5$ V, and it can be observed that beyond this voltage the modulation rate is approximately constant. Furthermore, the maximum estimated modulation rate is at a frequency of $f = 1.89$ THz and is found to be above 7 %, however, Pala et al. suspect that the actual modulation rate is much higher, but that the measurements were limited by the slow detector speed. Thus the results obtained in this work is promising for the use of grating-gate structures on an AlGaN/GaN-based HEMT.

In [44] the measurement of the resonant frequency in the large-area grating-gate AlGaN/GaN-based HEMTs is expanded to consider the dependence of transmission at the resonant frequency on temperature. The AlGAN/GaN HEMT used in this study was the same as in [3] with an AlGaN barrier layer thickness of $d = 28 \pm 2$ nm. In this study a single grating-gate design with a gate finger length of 1.15 µm and gate finger spacing of 0.35 µm was used, thus resulting in a period of 1.5 µm, and an active area of 1.6×1.7 mm^2.

The transmission spectra were measured at temperatures of 77 K, 120 K, 170 K, and 295 K. Fig. 4.12(a) shows the transmission spectra as a function of frequency for the four different temperatures at an applied gate voltage of $V_{\mathrm{g}} = 0$ V.

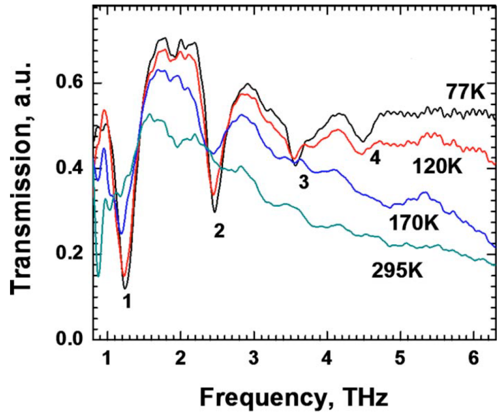

Figure 4.12. Transmission as a function of frequency at applied gate voltage of V_g = 0 V for temperatures of 77 K, 120 K, 170 K, and 295 K. Adopted from [44].

For 77 K, 120 K, and 170 K the resonant frequency of the fundamental, second, third and fourth harmonics are observed while at 295 K the higher harmonics are difficult to identify. For this temperature, a first harmonic can be seen at a frequency below 1 THz and a second harmonic can be seen near a frequency of 2 THz, both at frequencies below the ones measured at lower temperatures. This result shows that when lowering the temperature the resonant frequencies appear more clearly and, furthermore, the higher harmonics are only observed at the lowest temperatures.

This finishes the review of articles considering devices used for THz modulation by the use of SRRs, FSSs, or grating-gates on a HEMT. Based on the designs, dimensions, and results presented above the designs of the devices which are fabricated and used for measurements in this project will be chosen. The details on these are presented in the following chapter.

Chapter 5

Design and Fabrication of THz Modulators

This chapter provides details on design and fabrication of the THz modulators used for measurements in this project.

5.1 Design of THz Modulators

Based on the review of the literature in Chap. 4, the design of a grating-gate HEMT is chosen as the focus point, as the fabrication of such is simpler and more likely to succeed with the time frame of this project. Due to the fact that we do not have all the needed techniques for device fabrication in Aalborg, an agreement about collaboration with Twente University in the Netherlands was made. After consulting with them on their experience and available equipment the specific circular grating-gate configuration presented in Fig. 5.1 was designed by us. A circular structure was preferred over a square one to avoid having to introduce insulation between the independent devices. Instead, the source of each device acts as electrical screening from surrounding devices.

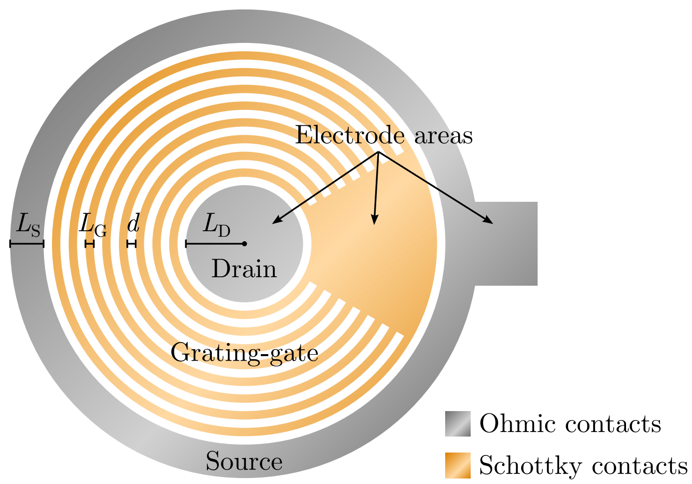

Figure 5.1. Illustration of the circular grating-gate design.

Similar large and small ring structures were designed, with the only difference being the size of the individual parameters. The design consists of a circular drain in the middle with radius, L_D, being at least 100 µm to make sure that the area is large enough for bonding of wires. This is surrounded by the grating-gate where the length of each gate ring is denoted by L_G while the spacing is denoted by d. All the gate rings are connected by a large electrode area on which it is possible to bond wires. On small designs there is one such electrode area for the gate rings while for the large designs there are two electrode areas connecting the gate rings, placed opposite each other, to ensure that the gate rings are internally connected. Lastly, one source ring is surrounding the gates and has a length, denoted by L_S, of 100 µm. As this is the outer ring it is not necessary to make this long enough for bonding wires directly on the ring. Instead a square area has been added on the side of the ring with a surface area of 500×500 µm^2 for the large ring designs and 200×200 µm^2 for the small ring designs. The details of the four different large ring designs are given in Tab. 5.1. Each ring has been assigned a name based on the system LR-L_G-d where LR stands for *large ring*. In the case of a single gate (SG) the name LR-SG will be used. A similar system will be introduced for the remaining designs and will be the names referred to further on.

Table 5.1. Overview of the dimensions of the large circular grating-gate structures. Here, L_D is the radius of the drain while L_G, d, and L_S are the lengths of the gate rings, gate ring spacing, and source ring, respectively.

Design	**L_D [µm]**	**L_G [µm]**	**d [µm]**	**L_S [µm]**	**#Gate Rings**
LR-2-2	200	2	2	100	745
LR-3-2	200	3	2	100	596
LR-30-30	200	30	30	100	47
LR-SG	200	2800	–	100	1

Due to the dimensions of the grating-gate HEMTs presented in [3] and [44] it is expected that LR-2-2 and LR-3-2 will provide the best results regarding THz modulation, however, LR-30-30 and LR-SG are still used as test structures and are thus also measured upon.

Besides these single large ring structures, 16 small ring structures are also connected in arrays, as seen in Fig. 5.2. In these arrays the ring structures are connected in parallel in such a way that the sources, drains, and gates are connected to their respective large electrodes by wires. Thus these large electrodes are possible to bond with wires and connect to power supplies.

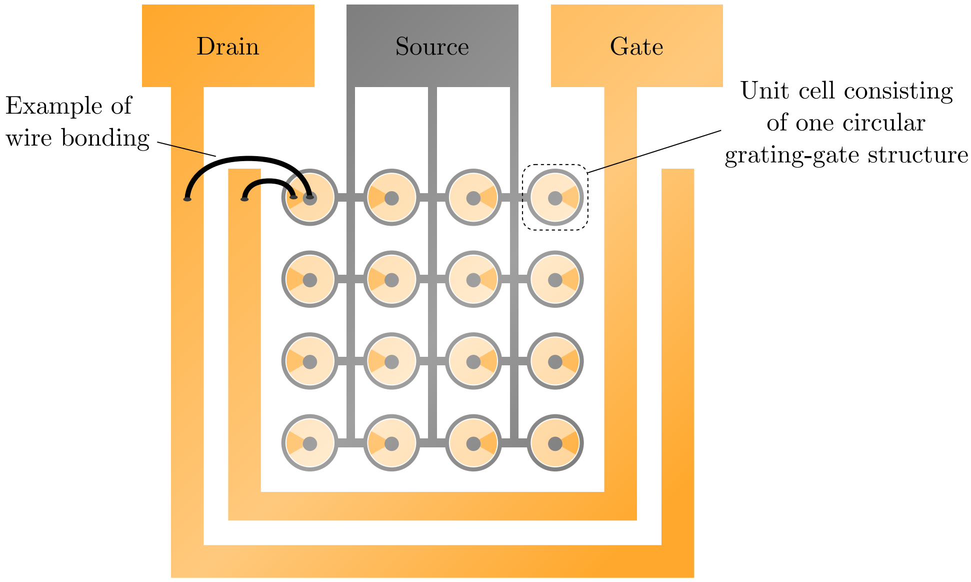

Figure 5.2. Illustration of the small circular grating-gate structures connected in an array.

Two arrays has been designed, each consisting of small ring structures of the same dimensions, and the details of the rings of these arrays are seen in Tab. 5.2. Here, the two arrays are assigned a name based on the system RA-$\mathrm{L_G}$-d, where RA stands for *ring array* as the details provided are those of one of the individual rings in each array.

Table 5.2. Overview of the dimensions of the small circular grating-gate structures which are connected in arrays. Here, L_D is the radius of the drain while L_G, d, and L_S are the lengths of the gate rings, gate ring spacing, and source ring, respectively.

Design	$\mathrm{L_D}$ [µm]	$\mathrm{L_G}$ [µm]	d [µm]	$\mathrm{L_S}$ [µm]	#Gate Rings
RA-2-2	125	2	2	100	51
RA-3-2	125	3	2	100	41

The length and spacing of the gate rings are the same as for LR-2-2 and LR-3-2, in the hope that modulation of the THz radiation will be successful. The expectation is that the single small ring designs will not provide a strong signal themselves, but that the connection of more enhances the signal, thus making it possible to measure. In this way, the results of RA-2-2 and RA-3-2 can be compared to the results of LR-2-2 and LR-3-2, respectively, in order to investigate if one of the designs provide better results than the other.

Lastly, several small ring structures were also designed separately such that these could be used as test structures. These are similar to the large ring structures in design, as the one seen in Fig. 5.1, however, the dimensions of the individual parameters summarised in Tab. 5.3 are smaller. These test structures are assigned a name based on the system SR-$\mathrm{L_G}$-d, where SR stands for *small ring*. In the case of a single gate and no gate the names SR-SG and SR-NG are used, respectively.

Table 5.3. Overview of the dimensions of the small circular grating-gate test structures. Here, L_D is the radius of the drain while L_G, d, and L_S are the lengths of the gate rings, gate ring spacing, and source ring, respectively.

Design	L_D [µm]	L_G [µm]	d [µm]	L_S [µm]	#Gate Rings
SR-2-2	125	2	2	100	51
SR-3-2	125	3	2	100	41
SR-5-5	125	5	5	100	21
SR-10-10	125	10	10	100	11
SR-20-20	125	20	20	100	6
SR-SG	125	200	–	100	1
SR-NG	125	–	–	100	0

These test structures will be used for the electrical characterisation of the sample, and are thus important for the purpose of ensuring a high quality of the sample.

5.2 Fabrication of THz Modulators

The THz modulators used for measurements in this project are fabricated in collaboration with Twente University in the Netherlands and consist of an AlGaN/GaN HEMT on a Si(111) substrate with the integrated circular grating-gate design. The substrates on which the HEMTs were grown were diced from high-quality GaN-on-Si wafers with approximately a 1.5 µm thick GaN layer, a 20 nm thick $Al_{0.2}Ga_{0.8}N$ film, and a 3 nm GaN capping layer. The source and drain ohmic contacts as well as the gate were patterned by photolithography using two separate masks designed in the open source program *L-Edit*. The ohmic contacts were deposited directly on top of the GaN capping layer, to make electrical connections to the 2DEG. These contacts as well as the large source electrode of the arrays consist of Ta/Al/Ta (10/280/20 nm) metal stacks. They were rapidly thermal annealed (RTA) at 550°C for 30 s in an N_2 atmosphere to form conductive TaN at the interface with GaN. The gate contacts were made of Ni/Au (25/125 nm) metal stacks which have not been exposed to any heat treatment. All the metal layers were deposited in an e-beam evaporator at a base pressure of 1.5×10^{-7} mbar.

All the LR and RA designs described in Sec. 5.1 were fabricated on one single chip of the size of 3×3 cm^2. Besides these six designs, which had the purpose of being used for THz spectroscopy measurements, the sample also had to include the small ring designs used for testing the electronic properties of the sample. There was a need for as many test structures as possible for probing of the electronic properties, and thus the sample was filled with as many structures as possible. Therefore, the six designs for the THz measurements of interest in this project were inserted and the remaining room was filled with small ring designs of different grating-gate periods. An overview of the sample is seen in Fig. 5.3, where the top left large ring is LR-2-2, the top right large ring is LR-3-2, the bottom right large ring is LR-30-30, and the bottom left large ring is LR-SG. Furthermore, the left of the arrays is RA-2-2 whereas the right array is RA-3-2.

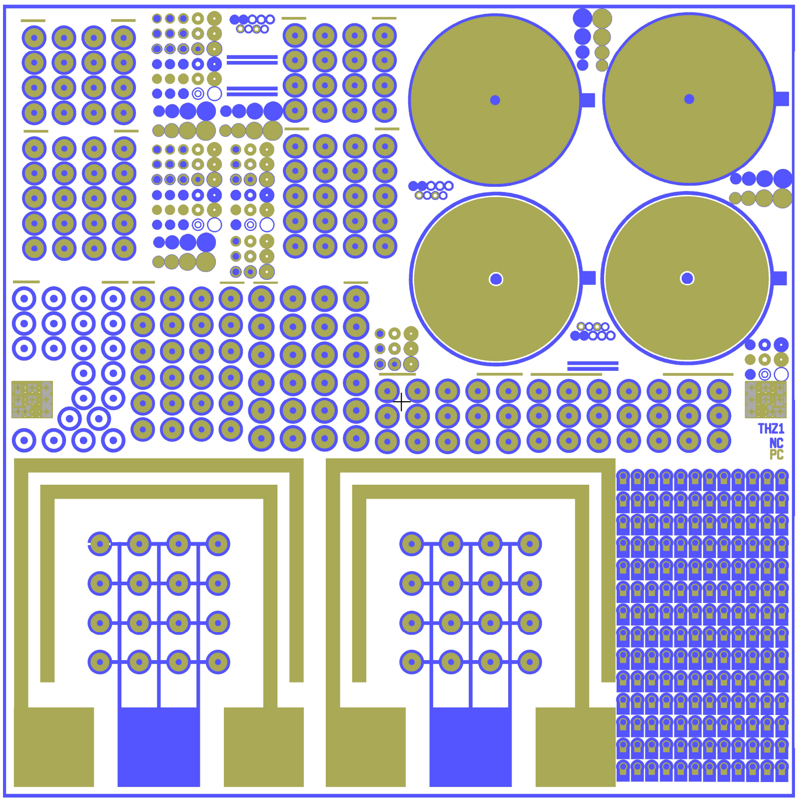

Figure 5.3. Illustration of sample design with a surface area of 3×3 cm^2.

In order to ensure that the fabrication of the individual structures was successful the sample was investigated under a microscope. Here it was evident that the fabrication of devices with gate rings on the scale of 2 µm did not succeed, as they were broken. This is seen in Fig. 5.4(a) which shows LR-2-2 and in Fig. 5.4(b) showing a SR-2-2, which is a small test ring similar to those of which RA-2-2 consists. Therefore, LR-2-2 and RA-2-2 will not be further investigated along with any test structures having the same grating-gate period.

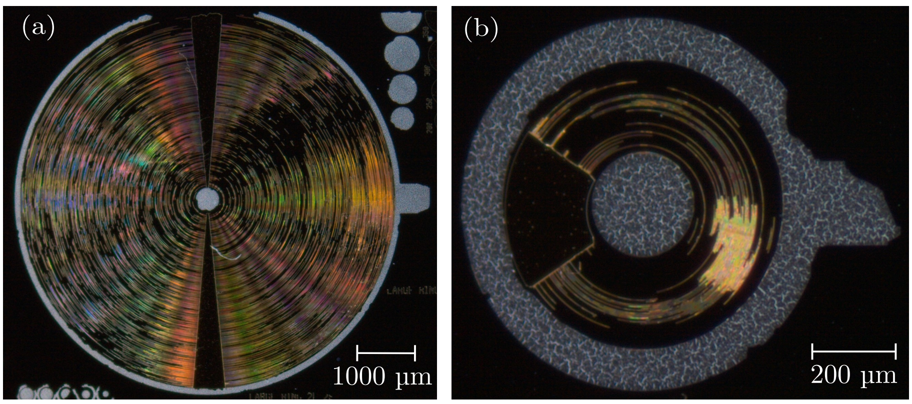

Figure 5.4. Microscope image of sample showing (a) LR-2-2 and (b) SR-2-2. These images reveal that the gate rings are broken due to the small period.

The gate rings of LR-3-2 appear to be successfully fabricated, however, due to the ring being located in the corner of the sample, it has been cut off at the top and the source contact on the right side seems to be damaged as seen in Fig. 5.5. Furthermore, the investigation of the device under the microscope indicates that there might be bad alignment of the contacts, meaning physical contact between the gate rings and the source and drain contacts, which may result in a short. Whether this is the case will be further investigated through electrical characterisation of the device.

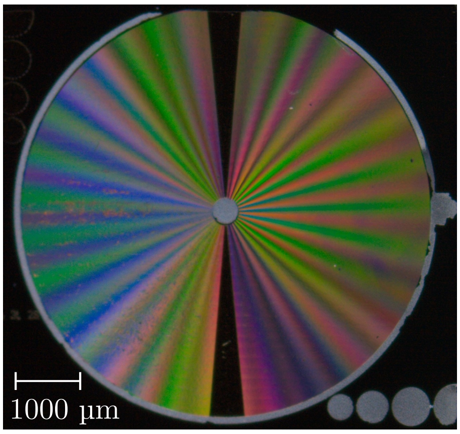

Figure 5.5. Microscope image of sample showing LR-3-2. The device is cut off at the top due to the location at the top of the sample.

Fortunately, most of the devices appear to be successfully fabricated and thus there are test structures of various grating-gate periods available for the electrical characterisation measurements of the sample. Examples of test structures SR-5-5, SR-20-20, and SR-SG are shown in Fig. 5.6(a), (b), and (c), respectively. From these images it is clear to see how both the drain and source ohmic contacts as well as the gate rings are intact and well-fabricated.

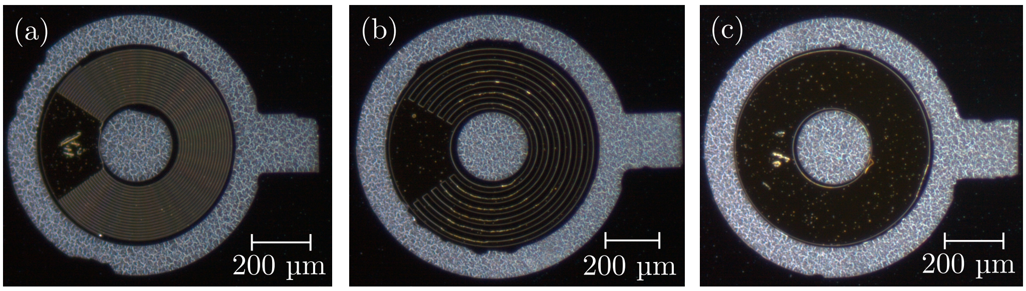

Figure 5.6. Microscope image of sample showing successfully fabricated test structures (a) SR-5-5, (b) SR-20-20, and (c) SR-SG.

Furthermore, also the remaining devices designed for the THz measurements appear to have been properly fabricated. In Fig. 5.7(a), LR-30-30 is shown along with a close-up image in Fig. 5.7(b). From these images it is clear to see how the gate rings along with the ohmic contacts are nicely fabricated and thus this device will be useful for both electrical characterisation and THz spectroscopy measurements. In Fig. 5.7(c) and (d), RA-3-2 and a close-up of one of the individual devices are shown, respectively. When looking at the individual ring structures of this device under the microscope it applies to most of them that there seems to be physical contact between the gate rings and the source and drain contacts, as the one shown in Fig. 5.7(d), which will lead to a short. However, every single device will be examined during the electrical characterisation to investigate of any short is present and thus ensure that the array can be expected to work properly during THz spectroscopy measurements where these devices are connected in parallel.

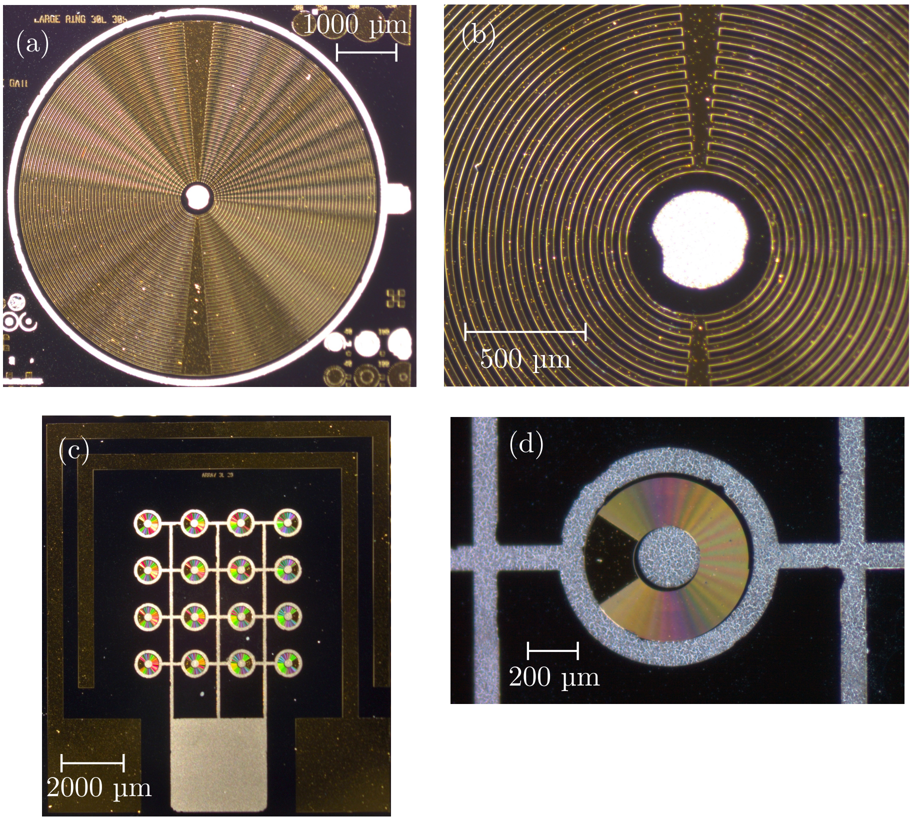

Figure 5.7. Microscope image of sample showing successfully fabricated (a) LR-30-30, (b) close-up of LR-30-30, (c) RA-3-2, and (d) close-up of an individual device of RA-3-2.

From the examination of the sample under the microscope it is thus expected that most of the test structures will be applicable for electrical characterisation where also LR-3-2 and LR-30-30 along with RA-3-2 will be tested. These results will reveal which of the large ring designs along with the array have the greatest potential to provide successful results during THz spectroscopy measurements.

The source, drain, and gate electrodes of the ring designs are on the micron scale, and thus it requires special equipment to bond these with wires which can then be connected to power supplies during THz spectroscopy measurements. Furthermore, as the wires must be as short as possible, the sample was cut into smaller pieces containing the relevant devices. Afterwards, it was attempted to bond 20 µm wide Au wires to the contacts. The bonding was successful to the gate terminals, which have a top Au layer. However, it appeared to be impossible to get any reliable bonds of Au wires with drain terminals having Ta film at the top. Thus, internally connecting the individual transistors of RA-3-2, shown in Fig. 5.7(c), turned out to be unsuccessful. It may still be possible to make individual electrical contacts to terminals of the large ring structure LR-30-30 shown in Fig. 5.7(a). However, this attempt requires design and fabrication of a special holder with tungsten probes. This solution will be further discussed in Sec. 7.2.1.

Chapter 6

Experimental Procedure

This chapter provides information on the equipment and experimental procedure utilised for measurements of the devices. It is divided into two parts; the first considering the electrical characterisation and the second considering the THz spectroscopy measurements.

6.1 Electrical Characterisation

The electrical characterisation measurements of the devices were performed using a Keithley 4200A-SCS Parameter Analyzer. This analyzer was connected to a three-probe station, where the sample was placed on the chuck of the probe station, and held fixed by suction creating vacuum on the backside of the wafer. The probe needles were then physically connected to the contacts of the devices on the sample. Due to the individual devices and contacts being on the µm-scale, the probe needles were carefully controlled by macro and fine needle adjustments while using the associated microscope. This was done to ensure good quality of the chosen devices as well as proper contact between the probe needle and device contacts before measurements were performed. An illustration of the probe station is shown in Fig. 6.1.

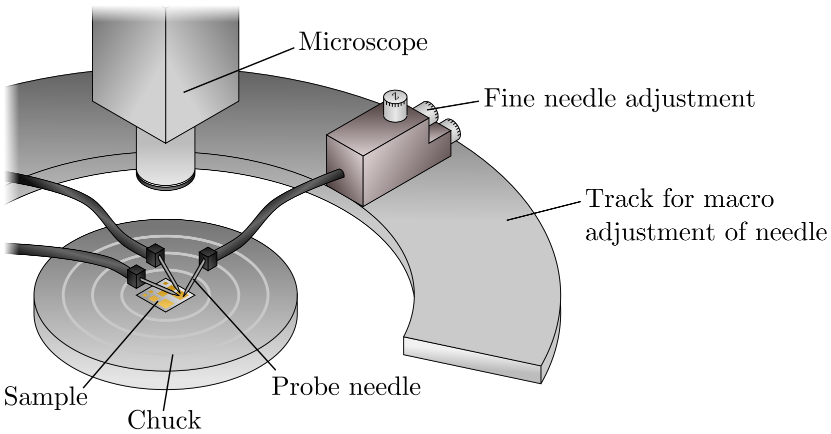

Figure 6.1. Illustration of probe station.

By assigning separate operation modes to the individual probes on the Keithley Parameter Analyzer, different electrical characterisation curves can be obtained. The *voltage linear sweep* operation mode is used to measure the source-drain current as a function of applied voltage between two contacts. The dependency between this *I-V* characteristic and the bias applied to the third contact can be measured using the *voltage step* operation mode. In this operation mode, individual *I-V* characteristic curves are measured for different applied voltages.

6.2 THz Spectroscopy

A TeraSmart compact THz-TDS from Menlosystems was available for THz spectroscopy measurements. This spectrometer consists of a THz emitter and a detector in each end, while lenses in between are used to focus the THz beam. In the middle there is room for the sample to be placed in a sample holder in such a way that the laser beam is focused on the relevant devices. An illustration of this set-up is shown in Fig. 6.2.

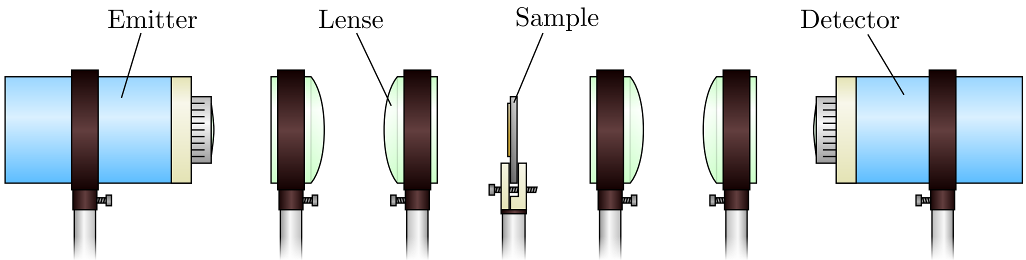

Figure 6.2. Illustration of THz-TDS set-up.

The range of frequencies of this spectrometer is 0.2−4.5 THz and it has a focal spot width of approximately 5 mm, which has been taken into consideration when designing the devices, for them to be at an appropriate scale. As it is a time-domain spectrometer the integrated Fourier transformation is used to transform the output of the measurements into the frequency-domain, where the intensity of the transmitted THz beam is given as a function of frequency. The output measurement is an average of 3000 takes and does thus ensure that the most accurate result is obtained. Before measuring on the devices it is necessary to take a reference measurement. This is due to many frequencies in the THz range being absorbed by water vapour in the surrounding atmosphere. Furthermore, the sample holder or the materials of which the devices consist may also impact the measurements.

Chapter 7

Results and Discussion

This chapter will focus on the experimental results obtained by performing measurements on the structures described in Chap. 5 using the equipment and techniques covered in Chap. 6. However, as the bonding of devices did not succeed it was inherently not possible to investigate the modulation properties of the devices through THz spectroscopy. Therefore, this chapter will mainly focus on displaying and discussing the electrical characteristics of the AlGaN/GaN sample and the individual devices. The main purpose of this electrical characterisation is to investigate which devices would have been suitable for THz modulation. Only structures which have a seemingly good geometrical quality will be studied, as the ones with bad alignments and too many defects would not have been suitable for THz modulation regardless of their electrical properties. Besides this electrical characterisation, the last section of this chapter will describe the attempts of performing THz spectroscopy measurements, as well as discuss the possible solutions to overcome the problematics regarding bonding of the devices.

Throughout this experimental chapter, the notation for the different device structures introduced in Chap. 5 will be utilised. The following illustration will recap this notation:

Structure type   Gate ring spacing in µm

SR-5-5

Length of gate rings in µm

There are three different structure types, namely the small rings (SR), large rings (LR), and ring arrays (RA), which can have different length and spacing of the gate rings, but also just have a single gate (SG) or no gate (NG). This means that the structure SR-5-5 is a small ring with a gate ring lengths and spacing of both 5 µm.

7.1 Electrical Characterisation of Devices

Performing electrical characterisation of the AlGaN/GaN-based devices is a necessity in order to ensure that they have the proper quality and functionality to be used as THz modulators. Throughout this section, various electrical characterisation techniques will be utilised in order to study a range of distinct electrical aspects such as the quality of the source, drain and gate contacts, as well as impact of structure geometry and the quality of the sample in general.

By measuring the output characteristics of a transistor device, which is the source-drain current as a function of source-drain voltage for different gate voltages, it is possible to investigate whether or not the device is able to regulate the concentration of charge carriers in the channel by tuning the gate voltage. In Fig. 2.5(a), which is results from [1], a proper output characteristic curve of an AlGaN/GaN HEMT is presented. From this curve it is directly seen that the maximum source-drain current is tunable by the gate voltage. This means that a 2DEG has been formed in the sample thus creating a conducting channel and, furthermore, that the concentration of electrons in this channel can be adjusted by an applied electric field from the gate contact. This also indicates that proper source and drain ohmic contacts have been constructed, which are electrically connected through the channel, whereas also a proper gate Schottky contact has been constructed, regulating the source-drain signal without disturbing it through a leakage. Therefore, obtaining results similar to the ones represented in Fig. 2.5(a) would be an indication of a generally good HEMT structure and AlGaN/GaN sample. Thus, one of the main focus points of this section will be to consider the output characteristics of the fabricated structures to discuss the quality of the structures, contacts, and sample.

The output characteristic curve for a SR-5-5 structure of good geometry is shown in Fig. 7.1, where it has been plotted on both a linear and logarithmic scale.

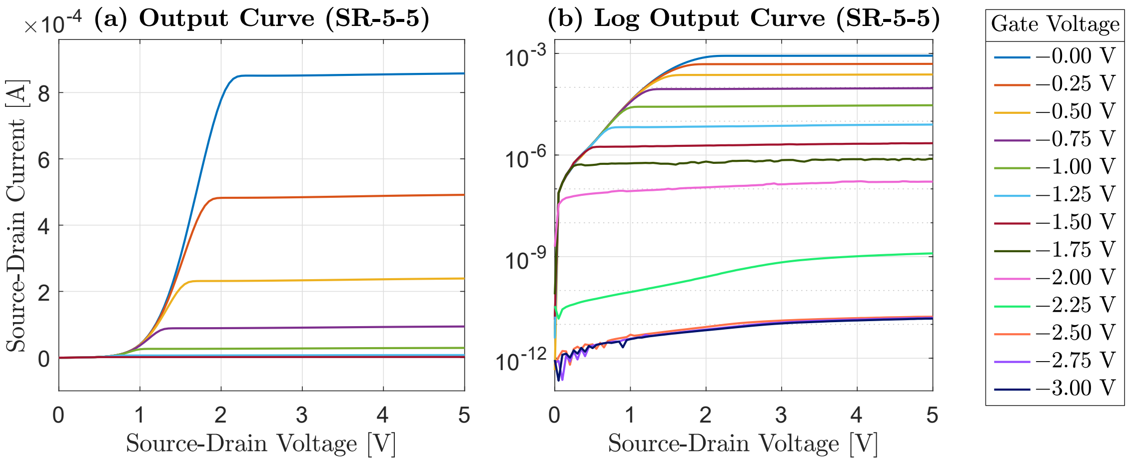

Figure 7.1. Output characteristic curve for a functional SR-5-5 structure, describing the dependency between source-drain current and voltage for specific gate voltages. This curve is plotted on both a (a) linear scale and (b) logarithmic scale.

From Fig. 7.1(a) it can be seen how SR-5-5 does not follow the exact same tendency as the HEMT in Fig. 2.5(a). One of the main differences is that for the SR-5-5, only an insignificantly small source-drain current flows for source-drain voltages below approximately 0.8 V, which results in the curve not showing a linear I-V dependency in the unsaturated region. A likely explanation for this is that the source and drain contacts are not fully ohmic. This means that a certain potential has to be applied in order to overcome the barrier and establish a flowing current. However, after this potential barrier has been overcome a seemingly linear dependency between source-drain current and voltage is present, before reaching the saturation region. Another important difference between

Fig. 7.1(a) and 2.5(a) is that the SR-5-5 does not show a linear dependency between saturation source-drain current and gate voltage, represented by decreasingly smaller steps in saturated source-drain current for linearly decreasing steps in the gate voltage. This could be due to a leakage current from the gate, which would gradually decrease the step-wise difference in source-drain current relative to what would be expected, as the gate voltage is negative. Even though the output characteristics deviate from those of an optimal HEMT, it is still obvious that a 2DEG is present and operates as a conducting channel between source and drain, and that the electron concentration in this channel is tunable by the gate voltage. This tunability of the channel is the most necessary and critical property of a HEMT for it to be used as a THz modulator. By further examining both Fig. 7.1(a) and (b), it is seen that the source-drain current is saturated for a source-drain voltage above approximately 2.3 V at V_g = 0 V, and that the 2DEG is completely depleted for a gate voltage of around −2.5 V and below. This means that the threshold voltage of the device lies closely above this value. However, the threshold voltage will be determined more precisely later on.

Identical output measurements were performed on different SR test structures, such as SR-3-3, SR-20-20, SR-SG, etc., all yielding similar results. This consequently means that the results obtained for SR-5-5 was not caused by random defects or the specific geometry of this structure. Moreover, the similar results across the single gate and grating-gate structures indicate that the grating-gate does not affect the transistor properties of the devices.

Another way of characterising the electrical properties of the different devices is through the transfer characteristic curve. This curve describes the source-drain current as a function of gate voltage for different source-drain voltages and is shown in Fig. 7.2 for SR-5-5.

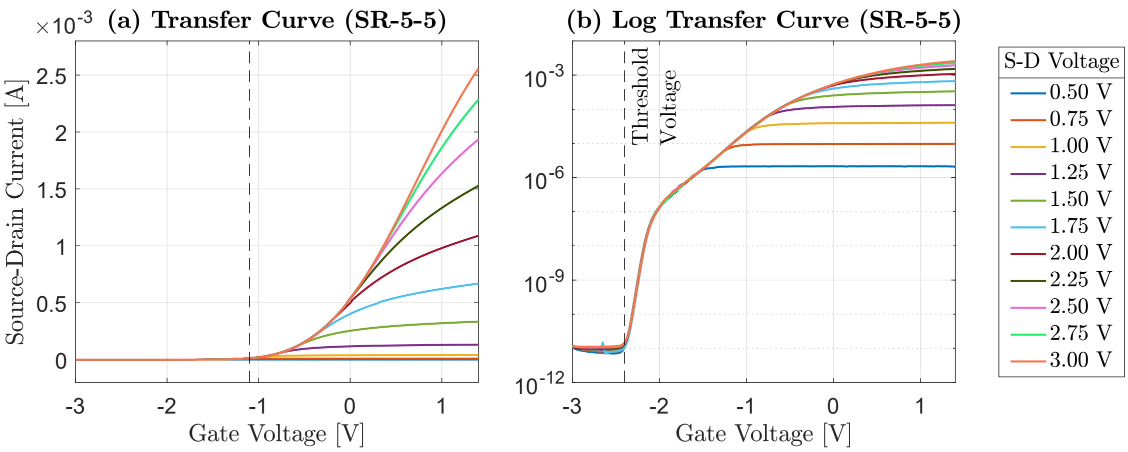

Figure 7.2. Transfer characteristic curve for the same functional SR-5-5 structure as in Fig. 7.1. This curve describes the dependency between source-drain current and gate voltage for specific source-drain voltages, and is plotted on both a (a) normal scale and (b) logarithmic scale.

From Fig. 7.2(a) it is again seen that the source-drain current is not linearly dependent on the gate voltage, unlike for the HEMT which transfer curve is shown in Fig. 2.5(b). It can, however, still be observed how the gate voltage is regulating the current through the channel which again illustrates the transistor-like behaviour of the device. The threshold voltage of the device can be precisely found as the gate voltage where the channel is pinched off, which by examining Fig. 7.2(b) is found to be around −2.4 V. Again, similar results were found for other SR structures. These structures are geometrically identical to the ones used in the RA structures, meaning that the their characteristics theoretically should be alike. However, since the RA-3-2 device is one of the main interests for THz experiments, each ring in this device will be studied separately to ensure that they all function properly.

Fig. 7.3 shows the output characteristic curves for five distinct and randomly selected ring structures within the RA-3-2 device. However, all rings were examined and all except one ring showed similar tendencies, hence these measurements are representative for 15 out of 16 ring structures.

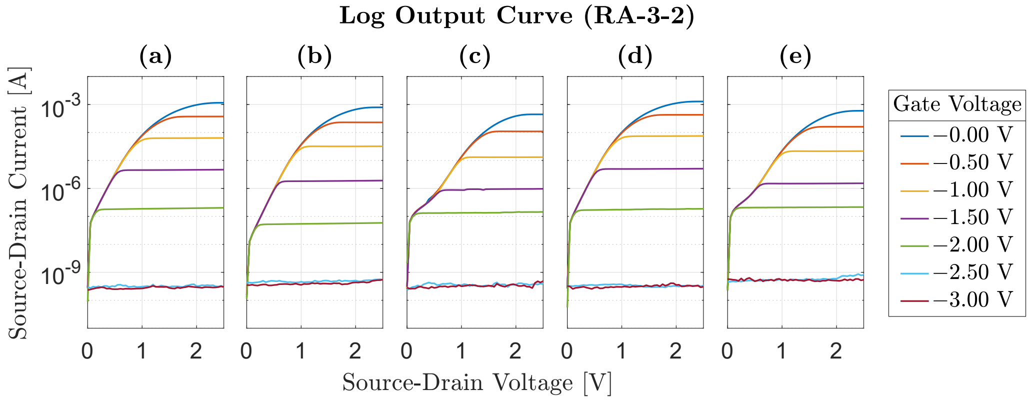

Figure 7.3. Output characteristic curves for five functional and randomly selected individual ring structures in the RA-3-2 device. All curves are plotted on the same logarithmic scale.

From these measurements it can be observed that the source-drain current for equivalent gate voltages varies differently across the structures. As all the rings are connected in a parallel circuit, each ring will experience an unequal current through the channel during THz experiments. However, in theory this should not be a concern as the plasma resonant frequency, given in Eq. (3.22), is independent on the electrical current. Hence, the varying dependency of the source-drain current of the rings on the gate voltage should not disturb the modulation capabilities of the device since they generate an identical plasma resonant frequency. Another concern arises from the fact that one of the 16 rings does not function as intended, which could be a cause of potential problems regarding THz modulation. The output characteristic curve of this ring is displayed in Fig. 7.4.

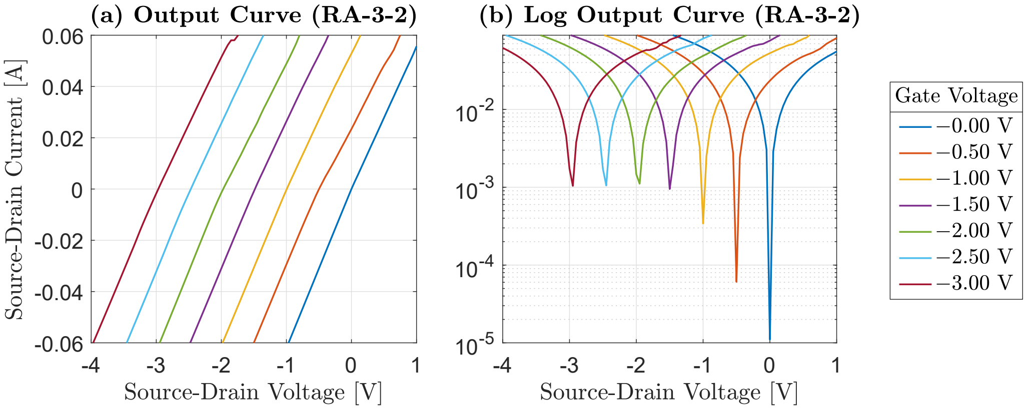

Figure 7.4. Output characteristic curve for the only non-functional individual ring in the RA-3-2 structure. This curve is plotted on both a (a) normal scale and (b) logarithmic scale.

The linear I−V characteristic of the curve present in 7.4(a) indicates that a short circuit has formed from the source to drain through the gate contact, most likely due to bad alignment of the contacts. Performing linear regression for V_g = 0 V reveals a resistance of 0.0591 Ω. Another strong indication that a short is present is that the applied gate voltage displaces the output curve by an equal voltage. The majority of the current applied to the array would potentially flow through the shorted ring, consequently ruining the functionality of the device due to all the functioning rings not being saturated. However, this problem can be overcome by disconnecting this broken ring from the rest of the array, which can simply be done by cutting the wire connecting the drain of this ring to the functioning ones. This reduces the amount of functioning rings of RA-3-2 to 15, which is still sufficient for the purpose of THz modulation. Unfortunately, as mentioned in Sec. 5.2, the RA-2-2 device was ruined due to unsuccessful fabrication of the narrow grating gates, thus these will not be electrically characterised.

The grating-gate LR structures are also of main interest since these are ideal for THz experiments. However, as for the RA-2-2 device, the LR-2-2 device was also unsuccessfully fabricated. From examining the LR-3-2 device using an optical microscope, it was observed to have a good quality gate structure. Unfortunately, the LR-3-2 device shows characteristics similar to the ones in Fig. 7.4, which means that a short is most likely present. A poor alignment of the contacts was observed and discussed in Sec. 5.2, which is the most probable explanation for this experimentally observed short.

Even though the LR-30-30 device is not expected to be appropriate for THz modulation due to the large grating-gate lengths and spacing, it is still of interest to study if any modulation effects can be obtained nonetheless. Therefore, the electrical characterisation of the LR-30-30 device is also still of interest. The output characteristic curve of LR-30-30 is shown in Fig. 7.5.

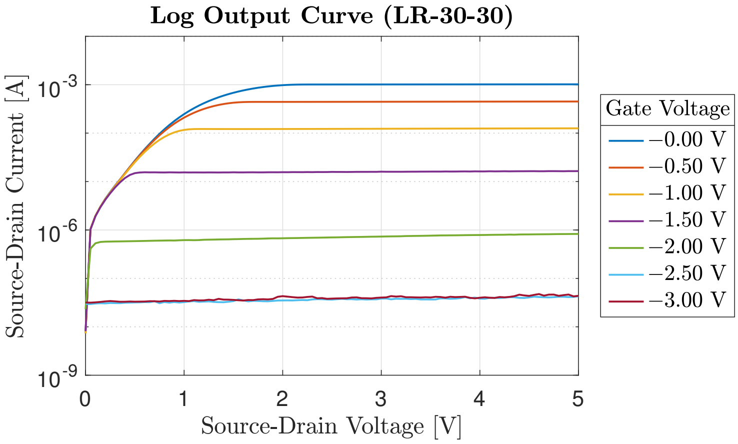

Figure 7.5. Output characteristic curve of the LR-30-30 structure plotted on a logarithmic scale.

From this curve it is seen that the LR-30-30 device has the same electrical tendencies as the SR devices, besides from a much higher cut-off source-drain current. However, as the device is not intended to be used for currents below this value, it will most likely not affect the THz experiments. Overall the conclusions drawn upon the SR-5-5 device can also be applied for LR-30-30.

7.1.1 Diode *I*-*V* Characteristic Measurements

The *I*-*V* characteristic curves between either the gate and source or the gate and drain of the individual devices on the sample have also been obtained. As the gate is a Schottky contact, the current can more easily flow from the source and drain than from the gate, and thus gate-source and gate-drain diodes are formed. It is expected that similar tendencies of the *I*-*V* characteristic curves should be obtained when using either the source or drain, provided that both contacts are of the same quality. This has been investigated for the SR-5-5 structure, where both gate-source and gate-drain diodes have been measured upon. The results of these measurements are seen in Fig. 7.6, showing the two logarithmic *I*-*V* characteristic curves, called diode curves.

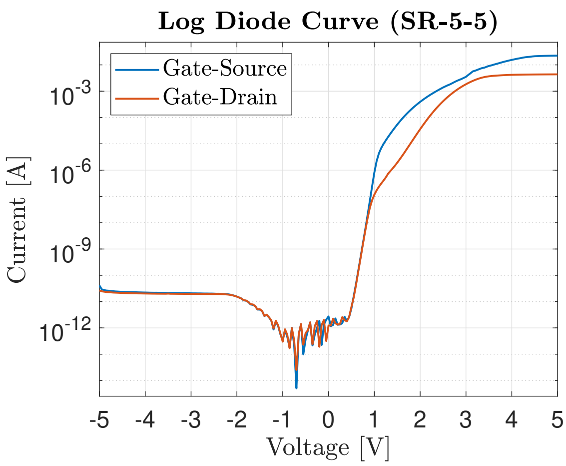

Figure 7.6. Gate-source and gate-drain diode curves for the SR-5-5 structure plotted on a logarithmic scale.

From these curves it is observed how the current can easily run in one direction while only a limited current can run oppositely. The two diodes are similar at reversed bias, both saturating at a low current for a voltage of approximately −2 V, which is the same voltage at which the 2DEG is depleted. This similarity is due to the gate being used for the two measurements is the same. It must be noted that even at reversed biases below the −2 V, a low current can still run. This may indicate that a low leakage current from the gate contact is present, as has been discussed above. On the other hand, when forward bias is applied the two diode curves saturate at different currents of 22.45×10^{-3} A and 4.367×10^{-3} A for the gate-source and gate-drain diode, respectively. This saturation current was expected to be the same, and thus this difference must be attributed to differences in the quality or size of the source and drain contacts, which have proven to not be perfectly ohmic. However, both logarithmic diode curves of Fig. 7.6 show the same tendency and thus, as the purpose of this section is to illustrate the overall tendency, only the gate-source logarithmic diode curves will be utilised in the further analysis.

Next, the gate-source logarithmic diode curves of several of the structures will be presented and compared. These structures are the small test rings SR-SG, SR-5-5, and SR-20-20 as well as the large ring LR-30-30. The results are seen in Fig. 7.7.

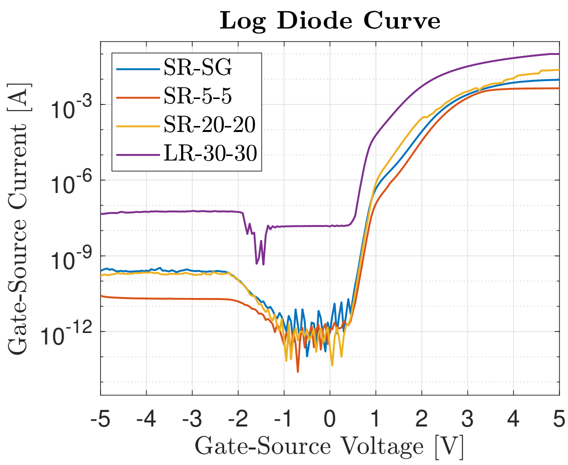

Figure 7.7. Gate-source diode curve for the SR-SG, SR-5-5, SR-20-20, and LR-30-30 structures, all plotted on a logarithmic scale.

Here, it is observed that the test structures all demonstrate typical diode behaviour with saturation currents in the range of 10^{-3} A at a forward bias while they all saturate at a reverse bias of approximately −2 V. The most noticeable difference between these three structures is that the saturation current for the reverse bias is lower for the SR-5-5 structure, which may be attributed to the higher quality of the gate allowing for a smaller current to run in this direction. A more significant deviation from the other diode curves is seen for the LR-30-30 structure. Generally, this structure displays a higher current level than the test structures, especially under reverse bias conditions. However, the saturation of the reverse current happens at a reverse voltage of approximately −2 V, as observed for the other structures. This result is in agreement with the output curves discussed above, where the current measured at complete depletion of the electron gas is significantly higher for LR-30-30 than for SR-5-5 or any of the individual ring structures in RA-3-2. However, the diode curve of LR-30-30 along with the diode curves of the three test structures show a tendency typical for diodes fabricated on HEMTs [45]. The results presented in Fig. 7.7 can be confirmed to display the expected tendency by comparison with the results presented in [45]. These results have been obtained by the same group which have fabricated the HEMTs used for measurements in this project, and thus the grown AlGaN/GaN samples are identical. As the purpose of the measurements in [45] was to investigate how the deposition temperature of a pure boron barrier layer between the GaN capping layer and the Al contact affects the diode current before and after annealing the sample at 400°C for 30 min in N_2 atmosphere, the exact values of diode current cannot be directly compared. Therefore, the purpose of this comparison is to confirm that the tendency observed in Fig. 7.7 is as can be expected. Thus, the results of the diode *I-V* characteristics obtained in [45] after annealing of the sample at 400°C for 30 min in N_2 atmosphere are shown in Fig. 7.8.

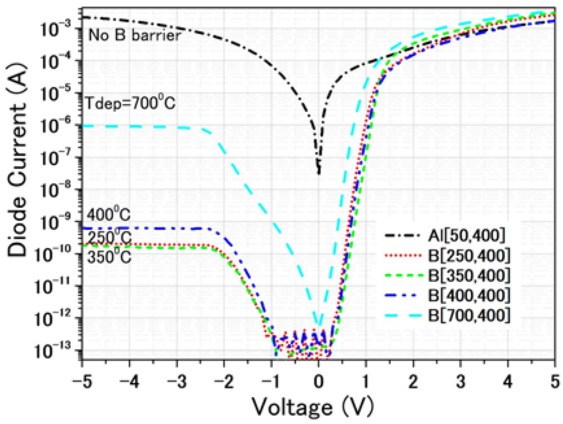

Figure 7.8. Diode curve of HEMTs fabricated on AlGaN/GaN samples identical to the one utilised in this project. A pure B barrier layer between the GaN capping layer and the Al contact has been deposited at varying temperatures. The sample has been annealed at 400°C for 30 min in N_2 atmosphere. Adopted from [45].

By comparing this result with that of Fig. 7.7 it is clear that the tendency of the diode current as a function of applied voltage is the same. The saturation current at reversed bias depends on the conditions under which the individual diode is fabricated, however, saturation happens at a voltage of −2 V, which is the bias at which the 2DEG is depleted. This observation is similar to that made for the sample measured upon in this project, as must be expected since the AlGaN/GaN samples utilised are identical. Furthermore, the saturation currents at a forward bias, independent of deposition temperature of the boron buffer layer, are in the range of 10^{-3} A, as is the case in Fig. 7.7. Based on this comparison it is deduced that the tendency of the diode curves seen in Fig. 7.7 is as can be expected.

7.1.2 Determining the Contact Resistance

In the previous section, the characteristics of the gate contacts were analysed in order to determine their quality. This section will focus on the source and drain contacts, which have earlier been determined to not be completely ohmic, however, they still show a linear ***I-V*** relation before reaching the saturation of the 2DEG. For this interval of linear tendency it is possible to find the associated resistance, given by the inverse of the slope. This resistance is a sum of the contact resistance of the source and drain as well as the resistance present in the 2DEG, as illustrated in Fig. 7.9.

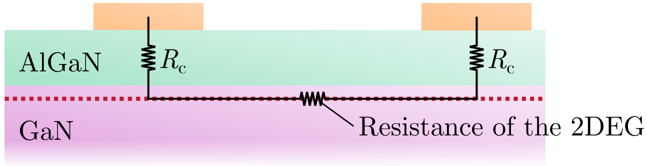

Figure 7.9. The resistances present in the circuit between the source and drain contacts of an AlGaN/GaN-based HEMT.

The contact resistance can be determined by investigating the total resistance between two contacts as a function of the distance between them, d_c [46]. In theory, this relation should be described by a linear function where the intersection coefficient describes the sum of contact resistance for the two contacts, hence the contact resistance can be found as half of the intersection coefficient.

The contact resistance is highly dependent on the size of the contact area. In this project, all the HEMT devices are based on a circular design. These are not ideal for these kind of contact resistance measurements, as the contact areas of the ring contacts in these circular structures vary. Therefore, additional test contacts were fabricated on the sample, in order to allow for proper contact resistance measurements. An optical microscopy image of these test contacts are shown in Fig. 7.10.

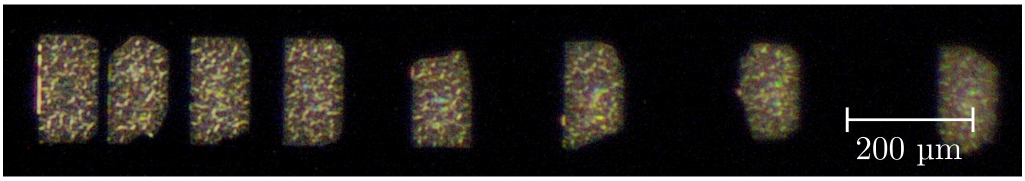

Figure 7.10. Microscope image of test contacts used for determining the contact resistance.

These test contacts were fabricated along with the source and drain contacts of the ring structures, meaning that they have similar metal stacking, chemical composition, and electrical properties. The dimensions of these contacts were design to be L = 100 µm and W = 180 µm. However, as can be seen in the image, the size of the contacts varies slightly due to non-perfect fabrication. The I-V characteristic between contact 1 and 2, from the left in Fig. 7.10, is seen in Fig. 7.11.

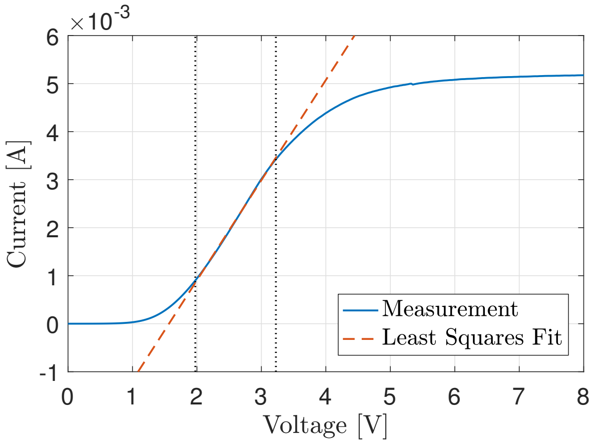

Figure 7.11. Measurement of the ***I-V*** characteristic between contact 1 and 2, from the left in Fig. 7.10. A least square fit has been made on the linear segment of the ***I-V*** curve, yielding a resistance of 479 Ω.

This plot shows the same tendency as in Fig. 7.1(a) for $V_g = 0$ V, again indicating that the contacts are not completely ohmic. The linear segment of the curve has been framed with dotted lines, and for data points within this interval a least squares fit has been made. The inverse slope of this fit yields a resistance of 479 Ω between these two contacts, which have a contact distance of 20 µm. A number of similar experiments have been performed on different combinations of contacts, yielding a relation between total resistance and contact distance. This experimental relation is shown in Fig. 7.12.

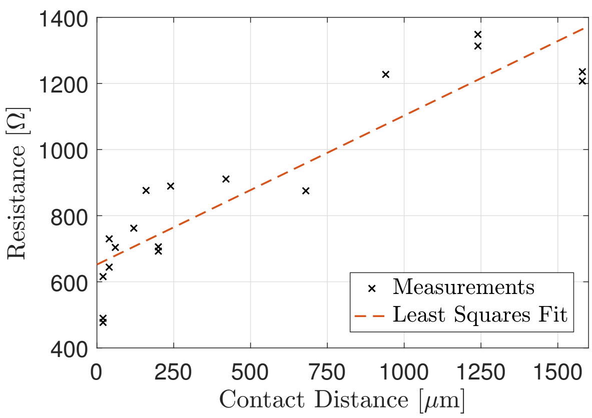

Figure 7.12. Experimental data describing the total resistance as a function of contact distance for the test contacts in Fig. 7.10. A least square fit has been made which yields a function given as $R_t = 0.451\ \frac{\Omega}{\mu m} \cdot d_c + 652\ \Omega$ and an r^2 value of 0.8335.

From this plot it is seen that the measurements have a high deviation from the sample mean, which is most likely due to the different shaping and contact area sizes of the test contacts. This deviation is also indicated by the low r^2 value of 0.8335. However, it is still observed that the measurements approximately follow a linear tendency. The total resistance can theoretically be described by

$$R_t = 2R_c + \frac{R_{sh}}{W}\, d_c, \tag{7.1}$$

where R_{sh} is the sheet resistance of the 2DEG [47]. The mean contact resistance for the test contacts is thereby given as 326 Ω, corresponding to half of the intersection coefficient for the linear fit. This value can be normalised with respect to the width of the contacts, in order to yield a quantity which can be compared to the literature. By multiplying with the width of 180 µm, a normalised contact resistance of 58.7 $\Omega \cdot$ mm is obtained. In [48] a normalised contact resistance of 0.06 $\Omega \cdot$ mm is obtained for Ta/Al/Ta (10/280/20 nm) contacts annealed at a temperature of 550°C, making them theoretically identical to the ones fabricated in this project. Thus, it can be seen that in our case the contact resistance is three orders of magnitude higher. However, in [49] a normalised contact resistance of approximately 36.3 $\Omega \cdot$ mm is obtained for Ta/Al (70/200 nm) contacts annealed at a temperature of 550°C. This value is much more comparable to the one obtained for the contacts fabricated in this project, which indicates that our case is not just a consequence of uncertainties during I-V measurements.

From Eq. (7.1) it can be seen that the slope of the fit in Fig. 7.12 must be equal to the sheet resistance divided by the contact width. Using this relation, the sheet resistance is calculated to be 81.1 Ω/sq., which is relatively low compared to the state-of-the-art values in the range from 225 to 350 Ω/sq. [26–31]. An explanation for this low sheet resistance could be that a leakage current flows through the substrate instead of the 2DEG channel, encountering a lower resistance and thus distorts the measured sheet resistance to yield a lower value. However, results such as the ones presented in Fig. 7.1 imply that the source-drain current can be fully controlled by the gate voltage, suggesting that the majority of the current flows through the 2DEG channel.

7.2 Attempts of THz Spectroscopy Measurements

As mentioned in the beginning of this chapter, THz spectroscopy measurements were not performed due to unsuccessful bonding of wires to the HEMT devices on the AlGaN/GaN sample. The unsuccessful bonding means that a source-drain current and gate voltage could not be applied to the devices during the spectroscopy measurements, which are necessities in order to obtain THz modulation. The main purpose of designing and fabricating these devices was to test their ability to modulate THz radiation. Since this could not be tested, it can only be concluded that the devices seem to have the proper HEMT properties which in theory should be appropriate for THz purposes. However, whether the circular grating-gate structures of the different devices allow for a coupling between the plasma waves in the 2DEG and the THz radiation cannot be concluded upon. The same can be said for the ability of the structures to generate a proper plasma wave resonant frequency in order to modulate THz radiation.

7.2.1 Alternatives to Wire Bonding

In order for the RA devices to function, it is required that all the gates, sources, and drains of the individual ring structures are internally connected. Therefore, unsuccessful bonding eliminates all opportunity for this device to work. However, the LR devices only need to be connected to the power supplies at three points in order to function, which allows for other possible solutions than wire bonding. Such a solution could be to construct a sample holder with integrated tungsten probe needles which are able to make electrical contact to the LR devices during THz measurements. However, a few problems arise from utilising such a solution. Firstly, the probe needles would be difficult to place correctly on the devices, since the gate, source, and drain areas have sizes of approximately 400 to 500 μm in width. Secondly, the needles might block some of the THz radiation from reaching the sample and thus reduce the area of the active region. Even though this method has some disadvantages and is difficult to execute, it would still have been interesting to try in order to obtain any THz spectroscopy measurements, regardless of the quality of these. However, as the last stretch of the project period was intensely used trying to bond wires to the devices, this technique was not attempted. If more time had been available, it would have been the next step in the further research.

Chapter 8

Conclusion

The purpose of this project was to design and fabricate THz modulators based on AlGaN/GaN HEMTs with a 2DEG conduction channel. The work was started by analysing appropriate theory and literature on the related topics. Namely, the fundamentals of FETs were studied with a focus on HEMTs. Critical parameters of HEMTs were investigated, here under the critical thickness of the AlGaN barrier layer for the 2DEG to form as well as the causes and consequences of defects and how the density of these can be reduced. Furthermore, the fabrication of ohmic contacts, here under the ideal metal stacking on AlGaN/GaN heterostructures was studied. Lastly, the formation of plasma waves in the 2DEG conduction channel of a FET on submicron scale was analysed. Under the right conditions the 2DEG can couple to THz radiation, making the HEMTs of high interest as THz devices of different regimes of operation.

Based on a review of numerous possible designs of THz modulators presented in the literature and an evaluation of the available equipment, circular grating-gate HEMT structures were chosen to be fabricated. Several large ring structures having different grating-gate periods were designed for THz modulation along with structures of smaller sizes for the purpose of electrical characterisation. The small ring structures were also designed in arrays, as it was expected that such devices could deliver a signal strong enough for THz spectroscopy measurements. The devices were fabricated on an AlGaN/GaN heterostructure grown on a Si(111) substrate, with ohmic contact and gate contact metal stacks of Ta/Al/Ta (10/280/20 nm) and Ni/Au (25/125 nm), respectively. Prior to performing the electrical characterisation, the devices were investigated using an optical microscope in order to identify the components successfully fabricated by photolithography to be used for electrical measurements. The test structures SR-3-2, SR-5-5, SR-10-10, SR-20-20, SR-SG, and LR-SG all appeared to be in good condition and thus suitable for electrical characterisation. The same can be said for the structures LR-30-30 and RA-3-2 which are also applicable for THz spectroscopy. The gate rings of the LR-3-2 device seemed to be in good shape, however, the quality of the device as a whole was questionable. Lastly, it was evident that the SR-2-2, LR-2-2, and RA-2-2 structures were not fabricated successfully, due to the small period of the grating-gates.

Characterisation of the SR-5-5 transistor structures revealed non-linear current behaviour for source-drain voltages below 0.8 V, which was an indication of the source and drain contacts not being completely ohmic. However, above 0.8 V there was a linear dependency between the source-drain current and voltage until the saturation current was reached, as expected from the literature. Furthermore, it was observed that the saturation current did not decrease linearly with decreasing gate voltage, which may be an indication of leakage through the gate. However, as demonstrated by the measurements, it was obvious that a 2DEG was present and could be controlled by the applied gate voltage. By analysing the transfer curve the threshold voltage of the device was determined to be −2.4 V. The electrical characterisation of the RA-3-2 array revealed that 15 out of 16 devices in the array showed similar *I*-*V* dependence and gate control to that of SR-5-5. The LR-3-2 structure revealed a short circuit between the source and drain, and thus this device was not measured further upon. The LR-30-30 device showed similar electrical characteristics to that of the SR-5-5 device, and thus was concluded to be useful for further investigation. The same was the case for the other successfully fabricated test structures.

As the next step of the electrical characterisation of the selected successfully fabricated devices, gate-source and gate-drain diode ***I-V*** dependencies were obtained. For the SR-5-5 devices the same dependencies were observed when using either the source or the drain. For both curves the current saturated at a reverse bias of approximately −2 V, corresponding to the voltage at which the 2DEG was completely depleted, while the saturation current in the forward bias was in the range of 10^{-3} A. The gate-source diode curves of the SR-SG, SR-5-5, SR-20-20, and the LR-30-30 structures were compared. All these showed similar tendencies in the diode curves with the only significant deviation being the generally higher current level of the LR-30-30 structure. The tendencies of these diode curves were typical for diodes fabricated on HEMTs and was thus comparable to the literature.

Lastly, the contact resistance of the ohmic contacts was found to be 58.7 $\Omega \cdot$ mm. This value is consistent with results obtained in literature describing metal stacks of Ta/Al (70/200 nm), however, it is higher than the best state-of-the-art values, indicating that the produced contacts are not of top quality. From the same measurements, the sheet resistance of the 2DEG was determined to be 81.1 Ω/sq., which was significantly lower than the state-of-art values. An explanation of this could be a leakage current through the substrate.

In order to perform THz spectroscopy measurements of the devices it was necessary to make wire bonding of the HEMT terminals to larger contact pads which could be used as connections for power supplies. Unfortunately, this procedure turned out to be unsuccessful for drain terminals as they were not covered by Au and, thus, became trouble points for Au wire bonding. Therefore, it was not possible to investigate if the fabricated devices were useful for THz modulation. However, based on the electrical characterisation it can be concluded that the devices exhibit transistor properties, where the 2DEG can be controlled by the gate voltage, which is a requirement for the devices to work as THz modulators.

8.1 Future Works

This section is devoted to present possible areas of further research of THz devices. This includes further investigation and optimisation of THz modulators as well as fabrication of THz emitters and detectors.

Considering the circular grating-gate devices fabricated and studied in this project, one needs to admit that the design and configurations were not very optimal as they were dictated by the available facilities and time frame. Thus, if more time was available, these could have been optimised to improve the structure of the electrical terminals making Au wire bonding possible, such that THz spectroscopy measurements could be performed. Moreover, the electrical quality of the metal stacks could be further improved in order to construct ohmic contacts with lower resistance, which would enhance the general functionality of the devices. Also the alignment of the lithography mask in sequential operations could have been improved to prevent electrical shorts of the small devices. However, as it is challenging to achieve a perfect alignment of different masks during photolithography on the scale of 1 μm, another solution to prevent shorts would be to increase the distance between the source and gate, and the drain and gate of the devices. The circular structures fabricated for this project were chosen in order to minimise current leakage between devices, without having to introduce additional insulation. However, introducing further insulation, such as a dielectric material, between the devices would undoubtedly improve the electrical screening even more. If such construction of insulation barriers could have been realised, also parallel grating-gates, as those presented in Sec. 4.3, could have been fabricated in the attempt of obtaining the best possible results on THz modulation.

Besides improving the already developed designs, a further and more extensive experimental research on these would also be of interest. Plasmon excitations in a magnetic field, known as magnetoplasmons, show resonance at THz frequencies in large-area grating-gate HEMT structures, as reported in [50]. Thus, this could be a topic of further study of the grating-gate HEMT structures as THz modulators. Furthermore, it would also be interesting to fabricate THz modulators based on metamaterial SRRs and FSSs integrated on HEMTs, as those described in Secs. 4.1 and 4.2. However, these designs are more advanced and require a more challenging fabrication process, ensuring that these metamaterial structures are integrated in the HEMTs.

It would also be interesting to study other applications of the 2DEG in HEMTs for THz devices. One such application is THz emission as obtained in [51–55], which requires a short electron channel and submicron gate length. Thus, the size of the emitters must be smaller than modulation devices in order to obtain THz emission. Another application is THz detection as investigated in [56–60], which can be obtained by both short and longer electron channels. Whether it is a resonant or nonresonant (broad band) detector depends on the parameters $\omega\tau$ and $s\tau/L$, where L is the channel length. Thus, if $\omega\tau \gg 1$ it is a resonant detector, meaning a short channel with $s\tau/L \gg 1$, whereas if $\omega\tau \ll 1$ it is a nonresonant detector, meaning a longer channel with $s\tau/L \ll 1$ [8, 40]. Lastly, it would be interesting to be able to have a frequency tunable device for which the resonant frequency is dependent on the applied gate voltage, as is done for an emitter in [53] and for a detector in [57].

Bibliography

[1] Jiandong Sun. *Field-effect Self-mixing Terahertz Detectors.* Springer, 1st edition, 2016. ISBN 978-3-662-48679-5.

[2] John F. Federici, Brian Schulkin, Feng Huang, Dale Gary, Robert Barat, Filipe Oliveira, and David Zimdars. THz imaging and sensing for security applications - explosives, weapons and drugs. *Semiconductor Science and Technology*, Vol. 20, pp. 266-280, 2005.

[3] Nezih Pala, Dmitry Veksler, Andrey Muravjov, William Stillman, Remis Gaska, and M. S. Shur. Resonant detection and modulation of terahertz radiation by 2DEG plasmons in GAN grating-gate structures. *IEEE SENSORS*, Conference, pp. 570-572, 2007.

[4] Ken B. Cooper, Robert J. Dengler, Nuria Llombart, Bertrand Thomas, Goutam Chattopadhyay, and Peter H. Siegel. THz imaging radar for standoff personnel screening. *IEEE Transactions on Terahertz Science and Technology*, Vol. 1, No. 1, pp. 169-182, 2011.

[5] David Shrenkenhamer, Saroj Rout, Andrew C. Strikwerda, Chris Bingham, Richard D. Averitt, Sameer Sonkusale, and Willie J. Padilla. High speed terahertz modulation from metamaterials with embedded high electron mobility transistors. *Optics Express*, Vol. 19, No. 19, pp. 9968-9975, 2011.

[6] Michael S. Shur and Victor Ryzhii. Plasma wave electronics. *International Journal of High Speed Electronics and Systems*, Vol. 13, No. 2, pp. 225-250, 2003.

[7] Michael Dyakonov and Michael Shur. Shallow water analogy for a ballistic field effect transistor: New mechanism of plasma wave generation by dc current. *Physical Review Letters*, Vol. 71, No. 15, pp. 2465-2468, 1993.

[8] Mikhail Dyakonov and Michael Shur. Detection, mixing, and frequency multiplication of terahertz radiation by two-dimensional electronic fluid. *IEEE Transactions on Electronic Devices*, Vol. 43, No. 3, pp. 380-387, 1996.

[9] Donald A. Neamen. *Semiconductor Physics and Devices: Basic Principles.* McGraw-Hill, 4th edition, 2012. ISBN 978-0-07-352958-5.

[10] Michael Shur. *Physics of Semiconductor Devices.* Prentice-Hall, 1st edition, 1990. ISBN 0-13-666496-2.

[11] Dieter K. Schroder. *Semiconductor Material and Device Characterization.* Wiley & Sons, 3rd edition, 2006. ISBN 978-0-471-73906-7.

[12] Giuseppe Greco, Ferdinando Iucolano, and Fabrizio Roccaforte. Ohmic contacts to gallium nitride materials. *Applied Surface Science*, Vol. 383, pp. 324-345, 2016.

[13] Seon Young Moon, Jun Ho Son, Kyung Jin Choi, Jong-Lam Lee, and Ho Won Jang. Indium as an effective ohmic contact to N-face n-GaN of GaN-based vertical light-emitting diodes. *Applied Physics Letters*, Vol. 99, No. 20, pp. 324-345, 2011.

[14] O. Ambacher, J. Smart, J. R. Shealy, N. G. Weimann, K. Chu, M. Murphy, W. J. Schaff, L. F. Eastman, R. Dimitrov, L. Wittmer, M. Stutzmann, W. Rieger, and J. Hilsenberg. Two-dimensional electron gases induced by spontaneous and piezoelectric polarization charges in N- and Ga-face AlGaN/GaN heterostructures. *Journal of Applied Physics*, Vol. 85, No. 6, pp. 3222-3233, 1999.

[15] O. Ambacher, B. Foutz, J. Smart, J. R. Shealy, N. G. Weimann, K. Chu, M. Murphy, A. J. Sierakowski, W. J. Schaff, L. F. Eastman, R. Dimitrov, A. Mitchell, and M. Stutzmann. Two dimensional electron gases induced by spontaneous and piezoelectric polarization in undoped and doped AlGaN/GaN heterostructures. *Journal of Applied Physics*, Vol. 87, No. 1, pp. 334-344, 2000.

[16] J. P. Ibbetson, P. T. Fini, K. D. Ness, S. P. DenBaars, J. S. Speck, and U. K. Mishra. Polarization effects, surface states, and the source of electrons in AlGaN/GaN heterostructure field effect transistors. *Applied Physics Letters*, Vol. 77, No. 2, pp. 250-252, 2000.

[17] I. P. Smorchkova, C. R. Elsass, J. P. Ibbetson, R. Vetury, B. Heying, E. Haus P. Fini, S. P. DenBaars, J. S. Speck, and U. K. Mishra. Polarization-induced charge and electron mobility in AlGaN/GaN heterostructures grown by plasma-assisted molecular-beam epitaxy. *Journal of Applied Physics*, Vol. 86, No. 6, pp. 4520-4526, 1999.

[18] Sten Heikman, Stacia Keller, Yuan Wu, James S. Speck, Steven P. DenBaars, and Umesh K. Mishra. Polarization effects in AlGaN/GaN and GaN/AlGaN/GaN heterostructures. *Journal of Applied Physics*, Vol. 93, No. 12, pp. 10114-10118, 2003.

[19] Raphael Brown, Douglas Macfarlane, Abdullah Al-Khalidi, Xu Li, Gary Ternent, Haiping Zhou, Iain Thayne, and Edward Wasige. A sub-critical barrier thickness normally-off AlGaN/GaN MOS-HEMT. *IEEE Electron Device Letters*, Vol. 35, No. 9, pp. 906-908, 2014.

[20] Anne Landgrebe-Christiansen and Jacob Nørkjær Schunck. Formation of Two-Dimensional Electron Gas in AlGaN/GaN Heterostructures, 2018. Available through the Aalborg University project library at www.aub.aau.dk.

[21] Stephen Pearton. *GaN and ZnO-based Materials and Devices (Springer Series in Material Science)*. Springer, 1st edition, 2012. ISBN 9783642235207.

[22] Hadis Morkoç. *Handbook of Nitride Semiconductors and Devices. Vol 1: Materials Properties, Physics and Growth*. Wiley-VCH, 2008. ISBN 9783527408375.

[23] Jr-Tai Chen. MOCVD growth of GaN-based high electron mobility transistor structures. Dissertation No. 1662, 2015.

[24] H. K. Cho, J. Y. Lee, G. M. Yang, and C. S. Kim. Formation mechanism of V defects in the InGaN/GaN multiple quantum wells grown on GaN layers with low threading dislocation density. *Applied Physics Letters*, Vol. 79, No. 2, pp. 215-217, 2001.

[25] V. N. Popok, T. S. Aunsborg, R. H. Godiksen, P. K. Kristensen, R. R. Juluri, P. Caban, and K. Pedersen. Structural characterization of MOVPE grown AlGaN/GaN for HEMT formation. *Reviews on Advanced Materials Science*, Vol. 57, No. 1, pp. 72-81, 2018.

[26] M. J. Manfra, N. G. Weimann, J. W. P. Hsu, L. N. Pfeiffer, K. W. West, and S. N. G. Chu. Dislocation and morphology control during molecular-beam epitaxy of AlGaN/GaN heterostructures directly on sapphire substrates. *Applied Physics Letters*, Vol. 81, no. 8, pp. 1456-1458, 2002.

[27] Wei-Ching Huang, Chung-Ming Chu, Yuen-Yee Wong, Kai-Wei Chen, Yen-Ku Lin, Chia-Hsun Wu, Wei-I Lee, and Edward-Yi Chang. Investigations of GaN growth on the sapphire substrate by MOCVD method with the different AlN buffer deposition temperatures. *Materials Science in Semiconductor Processing*, Vol. 45, p. 1-8, 2016.

[28] Xiaoliang Wang, Cuimei Wang, Guoxin Hu, Hongling Xiao, Cebao Fang, Junxi Wang, Junxue Ran, Jianping Li, Jinmin Li, and Zhanguo Wang. MOCVD-grown high-mobility $Al_{0.3}Ga_{0.7}N$/AlN/GaN HEMT structure on sapphire substrate. *Journal of Crustal Growth*, Vol. 298, pp. 791-793, 2007.

[29] Xiaoliang Wang, Guoxin Hu, Zhiyong Ma, Junxue Ran, Cuimei Wang, Hongling Xiao, Jian Tang, Jianping Li, Junxi Wang, Yiping Zeng, Jinmin Li, and Zhanguo Wang. AlGaN/AlN/GaN/SiC HEMT structure with high mobility GaN thin layer as channel grown by MOCVD. *Journal of Crystal Growth*, Vol. 298, pp. 835-839, 2007.

[30] Jr-Tai Chen, Ingemar Persson, Daniel Nilsson, Chih-Wei Hsu, Justinas Palisaitis, Urban Forsberg, Per O. Å. Persson, and Erik Janzén. Room-temperature mobility above 2200 $cm^2/V{\cdot}s$ of two-dimensional electron gas in a sharp-interface AlGaN/GaN heterostructure. *Applied Physics Letters*, Vol. 106, 251601, pp. 1-4, 2015.

[31] J. A. Smart, A. T. Schremer, N. G. Weimann, O. Ambacher, L. F. Eastman, and J. R. Shealy. AlGaN/GaN heterostructures on insulating AlGaN nucleation layers. *Applied Physics Letters*, Vol. 75, no. 3, pp. 388-390, 1999.

[32] Lei Pan, Xun Dong, Zhonghui Li, Weike Luo, and Jinyu Ni. Influence of the AlN nucleation layer on the properties of AlGaN/GaN heterostructure on (111)Si substrates. *Applied Surface science*, Vol. 447, pp. 512-517, 2018.

[33] Liang Wang, Fitih M. Mohammed, and Ilesanmi Adesida. Formation mechanism of ohmic contacts on AlGaN/GaN heterostructure: Electrical and microstructural characterizations. *Journal of Applied Physics*, Vol. 103, 093516, 2008.

[34] Fitih M. Mohammed, Liang Wang, Deepak Selvanathan, Hubert Hu, and Ilesanmi Adesida. Ohmic contact formation mechanism of Ta/Al/Mo/Au and Ti/Al/Mo/Au metallizations on AlGaN/GaN HEMTs. *Journal of Vacuum Science and Technology B*, Vol. 23, pp. 2330-2335, 2005.

[35] Xin Kong, Ke Wei, Guoguo Liu, and Xinyu Liu. Role of Ti/Al relative thickness in the formation mechanism of Ti/Al/Ni/Au ohmic contacts to AlGaN/GaN heterostructures. *Journal of Physics D: Applied Physics*, Vol. 45, 265101, 2012.

[36] B. Jacobs, M. C. J. C. M. Kramer, E. J. Geluk, and F. Karouta. Optimisation of the Ti/Al/Ni/Au ohmic contact on AlGaN/GaN FET structures. *Journal of Crystal Growth*, Vol. 241, pp. 15–18, 2002.

[37] Hyung-Seok Lee, Dong Seup Lee, and Tomas Palacios. AlGaN/GaN high-electron-mobility transistors fabricated through a Au-free technology. *IEEE Electron Device Letters*, Vol. 23, No. 5, pp. 623-625, 2011.

[38] Riccardo Degl'Innocenti, Stephen J. Kindness, Harvey E. Beere, and David A. Ritchie. All-integrated terahertz modulators. In Volker Sorger, editor, *Nanophotonics*, Vol 7, No. 1, pages 127–144. De Gruyter, 2018.

[39] M. Dyakonov and M. S. Shur. Plasma wave electronics for terahertz applications. In R. E. Miles, P. Harrison, and D. Lippens, editors, *Terahertz Sources and Systems*, NATO Science Series (Series II: Mathematics, Physics and Chemistry), vol 27, pages 187–207. Springer, Dordrecht, 2001. ISBN 9789401008242.

[40] Michael I. Dyakonov and Michael S. Shur. Plasma wave electronics: Novel terahertz devices using two dimensional electron fluid. *IEEE Transactions on Electronic Devices*, Vol. 43, No. 10, pp. 380-387, 1996.

[41] Minliang Liao, Jiawei Cong, Xiong Zhang, and Yiping Cui. Development of an electrically controlled terahertz-wave modulator. *Journal of Modern Optics*, Vol. 60, No. 20, pp. 1690-1695, 2013.

[42] Wenshan Cai and Vladimir Shalaev. *Optical Metamaterials: Fundamentals and Applications*. Springer, 1st edition, 2010. ISBN 9781441911520.

[43] Xiaoyu Zhang, Yuanyuan Xing, Qiang Zhang, Yanping Gu, Yao Su, and Chunlan Ma. High speed terahertz modulator based on the single channel AlGaN/GaN high electron mobility transistor. *Solid State Electronics*, Vol. 146, pp. 9-12, 2018.

[44] A. V. Muravjov, D. B. Veksler, V. V. Popov, O. V. Polischuk, N. Pala, X. Hu, R. Gaska, H. Saxena, R. E. Peale, and M. S. Shur. Temperature dependence of plasmonic terahertz absorption in grating-gate gallium-nitride transistor structures. *Applied Physics Letters*, Vol. 96, 042105, pp. 1-3, 2010.

[45] Shivakumar D. Thammaiah, John Lundsgaard Hansen, and Lis K. Nanver. Nanometer-thin pure B layers grown by MBE as metal diffusion barrier on GaN diodes, 2019. Presented at the 10th China Semiconductor Technology International Conference on March 18-19 2019 in Shanghai, China. To be published.

[46] Hyung-Seok Lee, Dong Seup Lee, and Tomas Palacios. AlGaN/GaN high-electron-mobility transistors fabricated through a Au-free technology. *IEEE Electron Device Letters*, Vol. 32, No. 5, pp. 111-113, 2011.

[47] G. K. Reeves and H. B. Harrison. Obtaining the specific contact resistance from transmission line model measurements. *IEEE Electron Device Letters*, Vol. 3, No. 5, pp. 111-113, 1982.

[48] A. Malmros, H. Blanck, and N. Rorsman. Electrical properties, microstructure, and thermal stability of Ta-based ohmic contacts annealed at low temperature for GaN HEMTs. *Semiconductor Science and Technology*, Vol. 26, 075006, pp. 1-7, 2011.

[49] G. Greco, F. Giannazzo, F. Iucolano, R. Lo Nigro, and F. Roccaforte. Nanoscale structural and electrical evolution of Ta- and Ti-based contacts on AlGaN/GaN heterostructures. *Journal of Applied Physics*, Vol. 114, 083717, pp. 1-5, 2013.

[50] K. Nogajewski, J. Łusakowski, W. Knap, V. V. Popov, F. Teppe, S. L. Rumyantsev, and M. S. Shur. Localized and collective magnetoplasmon excitations in AlGaN/GaN-based grating-gate terahertz modulators. *Applied Physics Letters*, Vol. 99, 213501, pp. 1-3, 2011.

[51] W. Knap, J. Lusakowski, T. Parenty, S. Bollaert, A. Cappy, V. V. Popov, and M. S. Shur. Terahertz emission by plasma waves in 60 nm gate high electron mobility transistors. *Applied Physics Letters*, Vol. 84, No. 13, pp. 2331-2333, 2004.

[52] N. Dyakonova, A. El Fatimy, J. Łusakowski, W. Knap, M. I. Dyakonov, M.-A. Poisson, E. Morvan, S. Bollaert, A. Shchepetov, Y. Roelens, Ch. Gaquiere, D. Theron, and A. Cappy. Room-temperature terahertz emission from nanometer field-effect transistors. *Applied Physics Letters*, Vol. 88, 141906, pp. 1-3, 2006.

[53] A. El Fatimy, N. Dyakonova, Y. Meziani, T. Otsuji, W. Knap, S. Vandenbrouk, K. Madjour, D. Théron, C. Gaquiere, M. A. Poisson, S. Delage, P. Prystawko, and C. Skierbiszewski. AlGaN/GaN high electron mobility transistors as a voltage-tunable room temperature terahertz sources. *Journal of Applied Physics*, Vol. 107, 024505, pp. 1-4, 2010.

[54] Y. M. Meziani, H. Handa, W. Knap, T. Otsuji, E. Sano, V. V. Popov, G. M. Tsymbalov, D. Coquillat, and F. Teppe. Room temperature terahertz emission from grating coupled two-dimensional plasmons. *Applied Physics Letters*, Vol. 92, 201108, pp. 1-3, 2008.

[55] Yanqing Deng, Roland Kersting, Jingzhou Xu, Ricardo Ascazubi, Xi-Cheng Zhang, Michael S. Shur, Remis Gaska, Grigory S. Simin, M. Asif Khan, and Victor Ryzhii. Millimeter wave emission from GaN high electron mobility transistors. *Applied Physics Letters*, Vol. 84, No. 1, pp. 70-72, 2003.

[56] Jian-Qiang Lü and Michael S. Shur. Terahertz detection by high-electron-mobility transistor: Enhancement by drain bias. *Applied Physics Letters*, Vol. 78, No. 17, pp. 2587-2588, 2001.

[57] A. El Fatimy, S. Boubanga Tombet, F. Teppe, W. Knap, D.B. Veksler, S. Rumyantsev, M.S. Shur, N. Pala, R. Gaska, Q. Fareed, X. Hu, D. Seliuta, G. Valusis, C. Gaquiere, D. Theron, and A. Cappy. Terahertz detection by GaN/AlGaN transistors. *Electronics Letters*, Vol. 42, No. 23, pp. 1342-1343, 2006.

[58] W. Knap, V. Kachorovskii, Y. Deng, S. Rumyantsev, J.-Q. Lü, R. Gaska, M. S. Shur, G. Simin, X. Hu, M. Asif Khan, C. A. Saylor, and L. C. Brunel. Nonresonant detection of terahertz radiation in field effect transistors. *Journal of Applied Physics*, Vol. 91, No. 11, pp. 9346-9353, 2002.

[59] W. Knap, Y. Deng, S. Rumyantsev, J.-Q. Lü, M. S. Shur, C. A. Saylor, and L. C. Brunel. Resonant detection of subterahertz radiation by plasma waves in a submicron field-effect transistor. *Applied Physics Letters*, Vol. 80, No. 18, pp. 3433-3435, 2002.

[60] W. Knap, Y. Deng, S. Rumyantsev, and M. S. Shur. Resonant detection of subterahertz and terahertz radiation by plasma waves in submicron field-effect transistors. *Applied Physics Letters*, Vol. 81, No. 24, pp. 4637-4639, 2002.